Magnetostratigraphy and stable isotope stratigraphy of the middle-Eocene succession of the Ainsa basin (Spain): new age constraints and implications for sediment delivery to the deep waters

Charlotte Läuchli[a*§], Miguel Garcés[b], Elisabet Beamud[c], Luis Valero[a], Louis Honegger[a], Thierry Adatte[e], Jorge E. Spangenberg[e], Julian Clark[f], Cai Puigdefàbregas[b], Andrea Fildani[g], Eric de Kaenel[h], Teodoro Hunger[a], Andres Nowak[a], Sébastien Castelltort[a]

[a] *Department of Earth Sciences, University of Geneva, Rue des Maraîchers 13, 1205 Geneva, Switzerland*
** currently at Institute of Geological Sciences, Freie Universität Berlin, 12249 Berlin, Germany*
[b] *Department of Earth and Ocean Dynamics & Geomodels Research Institute, Universitat de Barcelona, Martí i Franquès, s/n, 08028 Barcelona, Spain*
[c] *Paleomagnetic Laboratory CCiTUB-ICTJA, Institut "Jaume Almera", C/ Solé i Sabarís s/n, 08028 Barcelona, Spain*
[e] *Faculty of Geosciences and Environment, University of Lausanne, Géopolis - CH-1015 Lausanne, Switzerland*
[f] *Equinor Research Center, Austin, Texas, USA*
[g] *The Deep Time Institute, P.O. Box 27552, Austin, Texas 78755-7552, U.S.A.*
[h] *DeKaenel Paleo-Research, Mont-sur-Rolle, Switzerland*

§ Corresponding author

Keywords
Chronostratigraphy
Magnetostratigraphy
Stable isotopes
Deep marine
Sequence stratigraphy
Eustatism

ABSTRACT

Stratigraphic cycles preserved in sedimentary successions are controlled by the interaction of tectonics, climate, sediment supply and sea-level variations. Understanding the influence of these drivers on sedimentary systems dynamics is crucial to understand and extract information from sedimentary archives. In the deep marine deposits of the Ainsa foreland basin (lower to middle Eocene, southern central Pyrenees, Spain), the origin of well-preserved cyclicity between channelized sandy submarine fans and hemipelagic deposits remains subject to debate because of the absence of chronostratigraphic constraints on high resolution geochemical proxies. Here, we contrast a combination of newly acquired and legacy geochemical datasets (carbon and oxygen stable isotopes, organic matter content, major and trace elements and the mineralogical composition of bulk hemipelagic sediments) tuned by a new age model to global “target” curves to discuss the possible drivers of the stratigraphic cycles found in the deep marine sediment gravity flow deposits of the Hecho group. Our new age model is based on magnetostratigraphic and biostratigraphic dataset acquired on a composite section going from the Banaston system to the distal deposits of the Sobrarbe deltaic complex. Four major polarity zones are identified in the studied succession covering the time span from C21n (lower members of the Banaston system) to C19r (Sobrarbe deltaic complex). Our age model is corroborated by the identification of the nannoplankton zone NP16 in the Guaso system (C20n).

* Corresponding author e-mail address: charlotte.laeuchli@fu-berlin.de (Ch. Läuchli)

Comparison between global carbon and oxygen isotope curves and local isotopic datasets show some differences, suggesting the preservation of a local signal modulated by eustatism, changes in the petrography and/or restriction in water circulation in the Ainsa basin. Yet, comparison of the stratigraphic record with global sea-level curves highlights that sands are mainly delivered to the basin during lowstands, pointing to the important role of eustasy even in an active foreland tectonic context. The exception to the rule is the Banaston member II, whose deposition during a sea-level highstand seems to be controlled by the growth of tectonic structures.

1. Introduction

Stratigraphic cycles that characterize sedimentary records can be detected in depositional environments from continental to deep marine sinks worldwide. According to sequence stratigraphy, sedimentary deposition is driven, through modulation of accommodation and sediment supply, by the interaction of (1) global sea-level and eustatic variations related to climate and global tectonics, (2) local/regional tectonics, and/or (3) sediment supply (itself linked to global climate and tectonics) (e.g. Schlager, 1993; Castelltort and Van Den Driessche, 2003; Covault and Graham, 2010; Romans et al., 2016). Thus, sedimentary records contain crucial information regarding past climate and environmental signals. Deep marine environments are perfect targets to study these signals since large volumes of sediment are continuously deposited in submarine fans where the preservation potential is high (Hessler and Fildani, 2019).

In deep marine siliciclastic environments, cyclic patterns can be detected in the alternation of coarse sediments deposits forming submarine fans and low energy hemipelagic environments (e.g., Weltje and de Boer, 1993). The drivers of these pulses of coarse sediments remain a question mark in the study of deep-sea successions. Sands delivered to slope, base of slope and deeper basin environments are traditionally linked to sea-level lowstands (Vail et al., 1977; Posamentier and Vail, 1988). However, new models have been proposed in which sands are delivered to deep water at all sea-level stands (e.g., Covault et al., 2007; Castelltort et al., 2017). A better understanding of the drivers of deep-sea sedimentation is necessary given the source-rock/reservoir nature of deep-water sand-shale alternations (Bouma et al., 1985; Piper and Normark, 2001).

The Ainsa basin, in the southern central Pyrenees (Spain), is an ideal site to study the drivers of stratigraphic-cyclicity and paleoenvironments over multi-millennial times scales as an entire source to sink system is preserved for the time slice of interest. During the lower to the middle Eocene, the Ainsa deep marine basin is situated between the Tremp-Graus (fluvio-deltaic sediments) and the Jaca (distal deep marine sediments) basins (Fig. 1; Clark et al., 2017). This basin is filled by very well preserved syn-tectonic sediments typical of a proximal deep basin with submarine fans and hemipelagic deposits of slope, base of slope and basin floor environments. The Ainsa succession is made of eight major Sediment Gravity Flow (SGF) systems, including Fosado, Los Molinos, Arro, Gerbe, Banaston, Ainsa, Morillo and Guaso (terminology after Mutti, 1983 and Pickering and Bayliss, 2009; Figs. 3 and 4). SGF systems were deposited during Ypresian and Lutetian (lower to middle Eocene) ages (Bentham and Burbank, 1996; Pickering and Corregidor, 2005; Payros et al., 2009; Castelltort et al., 2017; Cantalejo et al., 2020).

The sand-shale packages of the Ainsa basin have been extensively described and studied (e.g., Mutti, 1983; Mutti et al., 1985; Remacha and Fernández, 2003; Pickering and Corregidor, 2005; Heard and Pickering, 2008; Heard et al., 2008; Pickering and Bayliss, 2009; Pohl and McCann, 2014; Cantalejo and Pickering, 2014, 2015; Scotchman et al., 2015; Clark et al., 2017; Castelltort et al., 2017; Cantalejo et al., 2020) but one of the main issues in deciphering the relative roles of external forces on stratigraphic records remains the availability of a robust chronostratigraphic framework that could be used to tune geochemical proxies in the basin. From Fosado to Banaston SGFs, Castelltort et al. (2017) noted that the stratigraphic cycles detected in the Ainsa basin have periodicities of approximately 1 Myr (Million year). In Castelltort et al. (2017), the Fosado, Gerbe and Banaston sandy systems are interpreted as being controlled by eustasy and deposited during sea-level lowstands. The age of the Arro system is poorly constrained and the connection with eustatism remains difficult. In Castelltort et al. (2017), the Arro system was linked to enhanced sediment supply during a sea-level highstand. Detrital zircon (U-Th)/He ages for the Arro sandy system support the hypothesis of short-frequency tectonic or climatic pulse during the deposition of this system (Thomson et al., 2017). More recently, nannofossil Subzone NP14a was identified in the Arro SGF system that could be associated with both sea-level highstand or lowstand (Cantalejo et al., 2020). From Banaston to Guaso SGF systems, the relationship between sea-level, sediment supply, tectonic and climatic modulations causing siliciclastic deposition in deep marine environment remain poorly known and acknowledged. The main task of this study was thus to improve the chronostratigraphic constraints on the studied succession in order to tune newly acquired geochemical proxies. Several studies and age models based mainly on biostratigraphy (Jones et al., 2005; Pickering and Corregidor, 2005; Scotchman et al., 2015) and magnetostratigraphy (Holl and Anastasio, 1993; Bentham and Burbank, 1996; Mochales et al., 2012a; Cantalejo et al., 2020) exist in the Ainsa basin. To build on these existing datasets, three approaches were used conjointly: magnetostratigraphy, stable isotope stratigraphy and biostratigraphy. Magnetostratigraphy provides accurate time lines by means of correlation with the Geomagnetic Polarity Time Scale, but needs the support of external age constraints provided here by established magnetostratigraphies in neighbouring successions and biostratigraphy. Stable isotope stratigraphy allowed the comparison and tuning with target global curves tied to accurate age models (e.g., sea-level curves of Miller et al., 2005 and Kominz et al., 2008, global carbon and oxygen isotope records of Cramer et al., 2009 and Zachos et al., 2001). Isotope records additionally provide paleoenvironmental information on the deposits.

Magnetostratigraphy and stable isotope analysis were performed on three sections (Labuerda, Forcaz and Morillo de Tou; Figs. 4, 6 and 7) in the deep marine sediments of the Ainsa basin to provide together with existing isotope records in Castelltort et al. (2017) a new chronostratigraphic framework for a near complete profile in the Ainsa basin deep marine succession. This data set was complemented with new and existing biostratigraphic data to calibrate the magnetostratigraphy. In addition, we provide data on the total organic carbon content, the elemental and mineralogical composition of bulk sediments to constrain environmental conditions in the system.

2. Geological setting

2.1 The Pyrenean orogeny and the south Pyrenean peripheral basins

The formation of the Pyrenean mountain range began in the late Santonian (upper Cretaceous, age, ~84 Ma) with the asymmetric collision and partial subduction of the Iberian plate below the Eurasian one (Muñoz, 1992; Roure and Choukroune, 1998; Beaumont et al., 2000; Fillon and van der Beek, 2012; Mouthereau et al., 2014). The Pyrenees are conventionally subdivided in three structural zones, (1) the Axial Zone formed by an antiformal stack of Paleozoic basement, (2) the retro-wedge and foreland basins of the Northern Pyrenean Zone and (3) the pro-wedge and foreland basins of the Southern Pyrenean Zone (Séguret, 1972, Fig. 1). The different phases of deformation associated to the development of this asymmetric mountain range are here described focusing on the Southern Pyrenean Zone. Counterclockwise (~35°) rotation of the Iberian plate (Choukroune, 1992), synchronous with the opening of the Bay of Biscay, led to an extensional rifting context during the early Cretaceous. The extensional system was replaced at the upper Santonian by a stage of inversion tectonics with the

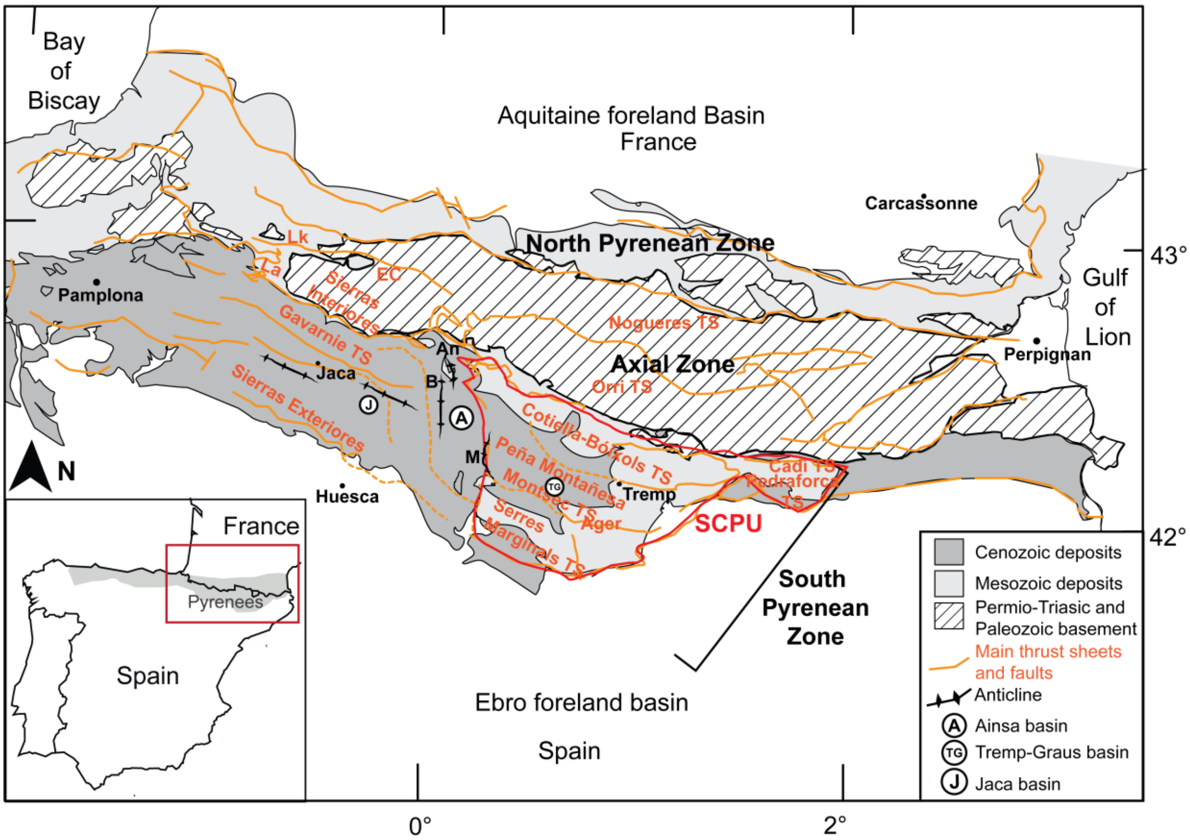

Figure 1. Main structural units of the South Pyrenean Zone and location of the Ainsa basin (modified from Mouthereau et al., 2014; Muñoz et al., 2013 and Labaume and Teixell., 2018) Abbreviations: An: Añisclo anticline; B: Boltaña anticline; EC: Eaux-Chaudes thrust; La: Larra thrust; Lk: Lakora thrust; M: Mediano anticline; SCPU: South-Central Pyrenean Unit; TS:Thrust Sheet.

reactivation of Mesozoic extensional fault and the development of the firsts Pyrenean thrust sheets (e.g., Cotiella-Bóixols thrust sheet, Muñoz et al., 2013, Fig. 1). Associated foreland basins formed at the front of these thrust sheets, were primarily filled by deep marine turbidites deposits (e.g., Vallcarga Formation, Puigdefàbregas et al., 1992). Coeval with the development of the Bóixols thrust sheet, shallow marine successions (Aren Sandstone Formation, Mey et al., 1968) and fluvial and lacustrine deposits (Tremp Group, Pujalte and Schmitz, 2005) were subsequently deposited in the eastern part of the Southern Pyrenean Zone. The asymmetrical collision between the Eurasian and the Iberian plate induced flow toward the WNW with the deposition of deep-water carbonate and siliciclastic sediments in the western part of the Southern Pyrenean Zone (Whitchurch et al., 2011, Thomson et al., 2019). During the Ilerdian stage (early Eocene), a major transgression flooded the southern basins leading to the deposition of the Alveolina Limestone Formation (Puigdefàbregas and Souquet, 1986). From the early to the middle Eocene, the Pyrenees underwent an acceleration of shortening rates and the exhumation of the Axial Zone (Whitchurch et al., 2011; Labaume and Teixell, 2018, Thomson et al., 2019). It led to the compartmentalization of the south Pyrenean basins into several parallel thrust-top structures forming the South-Central Pyrenean Unit (SCPU; parallel thrust sheets from north to south: Cotiella-Bóixols, Peña Montañesa-Montsec and Sierras Exteriores-Sierras Marginales; Puigdefábregas et al., 1992; Fig. 1). Geometries and facies distribution amongst the coeval piggy-back basins developed on top of these structures were controlled by the loading of the lithosphere and the emplacement of Mesozoic south verging faults (Puigdefábregas et al., 1992). The piggy back basin of Tremp, on top of the moderately subsiding hanging wall of the SCPU, was infilled by the fluvio-deltaic deposits of the Montanyana Group (Tremp-Graus basin, Figs. 2 and 3, Puigdefábregas et al., 1992). The sediments of the prograding fan of the Montanyana Group, were transported to the footwall of the Peña Montañesa-Montsec, and the Gavarnie thrust systems filling the distal Ainsa and the Jaca basins respectively (Muñoz et al., 2018, Figs. 1 and 2). The transfer of clastic sediment from proximal to distal environments was allowed by an east to west river drainage system (Nijman and Nio, 1975; Payros et al., 2009) linked to incised canyons (Atiart, Charo-Lascorz, Monclús and Formigales canyons) and channels along the marine lateral ramp (Clark et al., 2017). In the Ainsa and Jaca basins, the Hecho Group (Mutti, 1983), a succession of deep marine turbidites and hemipelagic deposits was accumulated between growing tectonic structures of the Mediano, Añisclo and the Boltaña anticlines forming the present-day segmentation between Tremp-Graus, Ainsa and Jaca basins (Figs.1 and 2).

The last stage of the development of the South-Central Pyrenean Unit is characterized by a decrease in subsidence rates due to the southward migration of the deformation and a general progradation induced by the development of the Pyrenean Axial Zone antiformal stack (Muñoz, 1992; Sinclair et al., 2005). From the upper Eocene to the Oligocene, successively shallow marine (Sobrarbe deltaic complex, Bartonian stage, Dreyer et al., 1999; Mochales et al., 2012a; Scotchman et al., 2015) and continental fluvial sediments (Escanilla Formation, Bentham et al., 1992; Michael et al., 2014, Vinyoles et al., 2019) were deposited in the basins. During the late Priabonian, the Tremp-Graus-Ainsa-Jaca basins were disconnected from the Atlantic sea, most probably as a consequence of the emplacement of the Basque-Cantabrian units in the west (Costa et al., 2010). The last tectonic activity related to the orogeny of the Pyrenees occurred during the late Oligocene- early Miocene (Puigfefàbregas, 1975; Rosenbaum et al., 2002; Labaume and Teixell, 2018).

2.2 The Ainsa basin

The Ainsa basin was developed from Lutetian to Priabonian times (Bentham and Burbank, 1996; Pickering and Corregidor, 2005; Payros et al., 2009; Mochales et al., 2012a; Cantalejo et al., 2020). Structurally, the basin is defined by its confinement between the lateral ramp of the Peña Montañesa-Montsec to the east, as well as the Gavarnie thrust and Boltaña anticline today to the west (Figs.1 and 2). As such, the Ainsa basin, open toward the deeper Atlantic waters to the west, was progressively syncline-deformed between three progressively growing anticlines (Mediano, Añisclo and Boltaña, Fig. 2).

The turbiditic succession of interest belongs to the Hecho Group (Mutti et al., 1972) and has been extensively studied (e.g., De Federico, 1981; Mutti et al., 1988; Barnolas and Gil-Peña., 2001; Pickering and Corregidor, 2005; Arbués et al., 2007; Pickering and Bayliss, 2009; Arbués et al., 2011; Pohl and McCann, 2014; Cantalejo and Pickering, 2014; Scotchman et al., 2015). All studies converge towards the interpretation that the Hecho Group was deposited below the shelf-edge of the Tremp-Graus basin into upper slope to base of slope depositional environments by channels and canyons (Atiart, Charo-Lascorz and Formigales canyons, Payros et al., 2009). The Tremp-Graus fluvio-deltaic system, feeding the Ainsa basin, was supplied in sediments by the reliefs of the early Pyrenean uplifts to the north, and the Ebro foreland basin to the south (Fig. 2; Gómez-Gras et al., 2016; Thomson et al., 2017).

At first-order, the deep marine stratigraphic series of the Ainsa basin are made of approximatively 4 km thick syn-tectonic deposits constituted by an alternation of sandy formations dominated by sediment gravity flow facies forming submarine fans, and marly formations. The latter are interpreted as slope deposits, levees deposits or distal turbidites. In more detail, the Hecho Group in the area of Ainsa is formed by eight subdivisions related to major unconformities and the migration of the axis of deposition of the sandy formations: Fosado, Los Molinos, Arro, Gerbe, Banaston, Ainsa, Morillo and Guaso Sediment Gravity Flow systems (SGFs, following the nomenclature of Pickering and Bayliss, 2009, Fig.3). Each Sediment Gravity Flow system is constituted by two to eight turbiditic

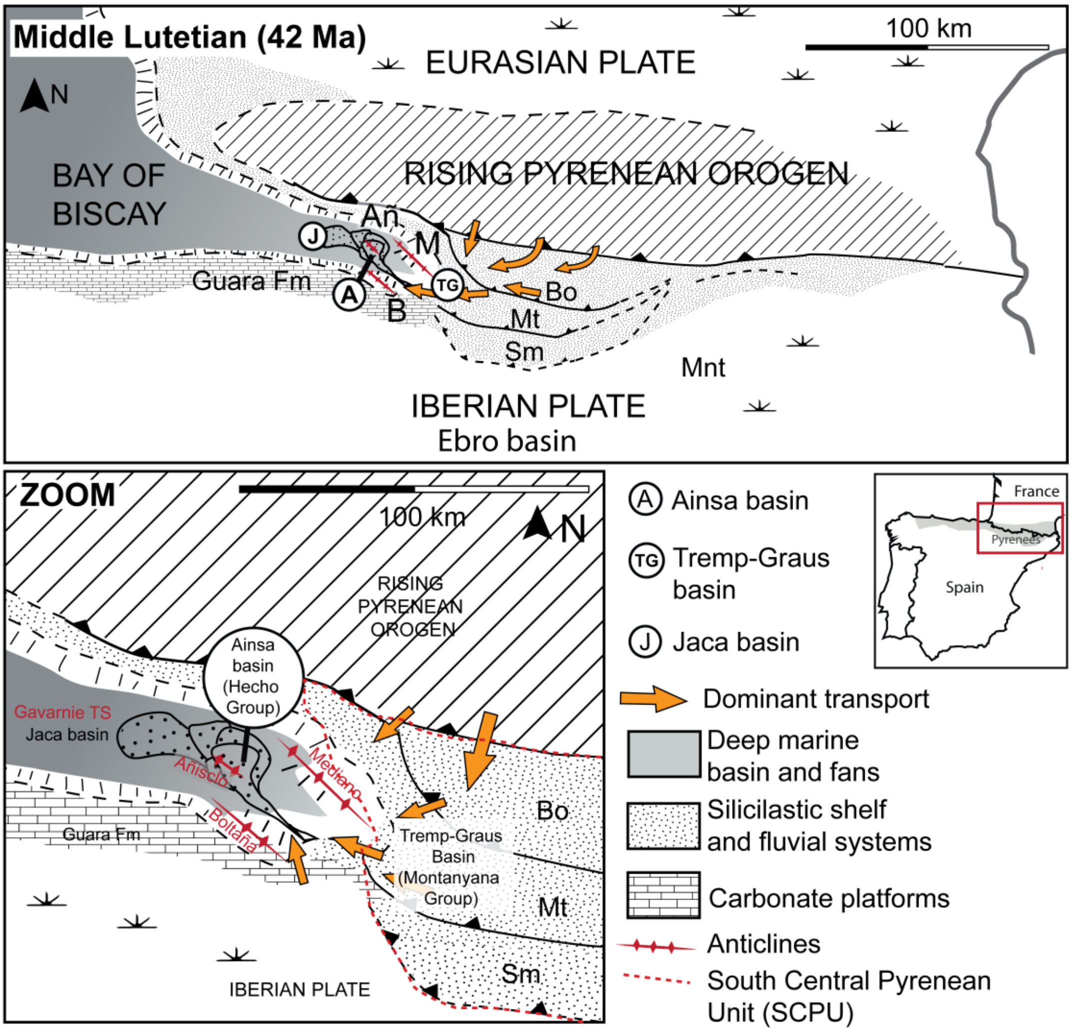

Figure 2. Paleogeographic reconstitutions of the Ainsa basin in the middle Lutetian (modified from Muñoz et al., 2013 and Castelltort et al., 2017). During the Lutetian, the Ainsa basin is largely underfilled and hosts slope and deep-water deposits of the Hecho Group. This period is also marked by the development of the Boltaña anticline controlling the geometry of the deposition in the basin. Note that the anticline has not rotated yet and is still in its initial position. Abbreviations: Añ: Añisclo anticline; B: Boltaña anticline; M: Mediano anticline; Bo: Cotiella-Bóixols thrust sheet; Mt: Peña Montañesa-Montsech thrust sheet; Sm: Serres Marginales thrust sheet.

sandbodies of hundreds of meters thick (Pickering and Bayliss, 2009) and large sequences of slope and hemipelagic marly deposits. Four major truncations are identified in the basin, the Atiart, Charo-Lascorz, Monclús and Formigales canyons (Payros et al., 2009 and Clark et al., 2017).

The deposition of the first sediment system of the Hecho Group in the area of Ainsa (Fosado) was estimated around 51 and 49 Ma (Scotchman et al., 2015). More precisely, the Atiart canyon located at the base of the Hecho Group deposits was dated between 50.2 and 50.5 Ma (Castelltort et al., 2017 and Clark et al., 2017). The deepening of the Ainsa basin from the shelf margin to the deep basin environment was associated to the enhanced subsidence of the footwall of the Peña Montañesa-Montsec trust sheet with respect to the South-Central Pyrenean Unit (Garcés et al., 2020).

The deposition of the lower Hecho Group (Fosado, Los Molinos and Arro SGF systems) was marked during the late Ypresian by the activation of the thrust system of La Fueba associated to the Peña Montañesa- Montsec thrust sheet development. The activation of La Fueba thrust system is coeval with major truncation in the Ainsa basin and induced deformation of the lower Hecho Group (Muñoz et al., 2013). In comparison, the upper Hecho Group (Gerbe, Banaston, Ainsa, Morillo and Guaso SGF systems) deposited during the Lutetian (Mochales et al., 2012a; Castelltort et al., 2017; Cantalejo et al., 2020) is less deformed despite the active tectonic evolution of the basin (Pickering and Corregidor, 2005). During the middle Eocene (early Lutetian), the Sobrarbe fold system was developed. The Gavarnie thrust sheet was deformed and the Ainsa basin transformed into a piggy-back basin. Two major anticlines separated by the Santa Maria de Buil syncline (Fig. 4) were formed displaying an ESE-WNW axis (Muñoz et al., 2013, Fig. 2) The Mediano anticline was developed between Tremp-Graus and Ainsa basins from the early Lutetian to the Bartonian (Poblet et al., 1998). The growth of this anticline is associated with the development of the smaller Añisclo anticline (Fernández et al., 2012; Muñoz et al., 2013). The Boltaña anticline separating Ainsa and Jaca basins was initiated at the middle Lutetian and ended in the early Priabonian (Muñoz et al., 2013). According to Heard et al. (2008), the development of the Boltaña anticline could have led to a partial restriction of water circulations between the Ainsa basin and the open ocean inducing periods of low oxygen levels in the Ainsa basin. As deformation proceeded, the basin underwent a progressive clockwise rotation (Mochales et al., 2012a) of 45° to 60° (Muñoz et al., 2013). As a result, paleoflows recorded at the base of the Ainsa basin succession are, at present time, generally oriented towards the NNW but were initially indicating west-oriented sediment transport. In contrast, towards the top of the succession, paleoflows are oriented towards the WNW closer to their initial directions. From the late Lutetian to the Priabonian, the basin was filled and, successively over-filled by the shallow marine Sobrarbe and the fluvial Escanilla Formations (Bentham, 1992; Mochales et al., 2012a).

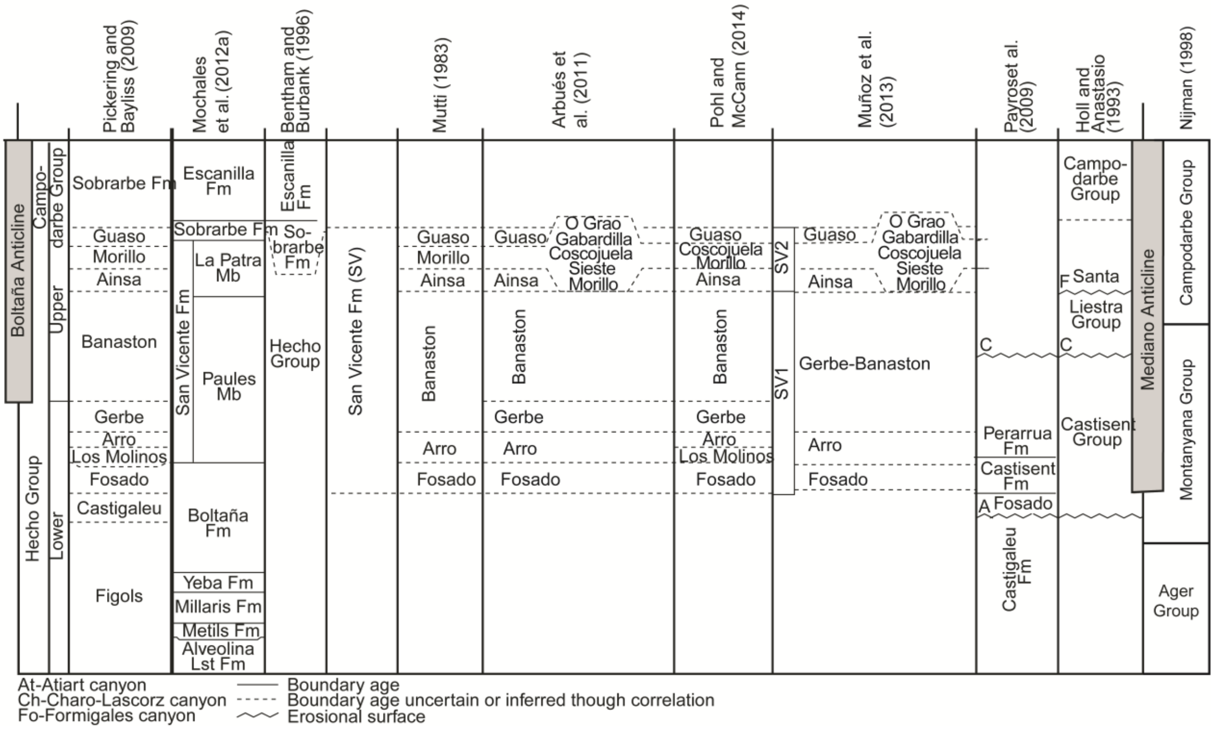

Figure 3. Synthesis of the different terminology used for the stratigraphic division and systems of the Ainsa basin (Modified from Scotchman et al., 2015 and Pohl and McCann, 2014)

3. Material and methods

A complete stratigraphic succession was sampled from Gerbe to Guaso SGF systems in the Ainsa basin for (1) magnetostratigraphy and (2) high resolution geochemical proxies. Two additional sites were sampled for biostratigraphy (see star, Fig. 4). The succession studied is a compilation of three sub-sections named Labuerda (1000 m), Forcaz (462 m) and Morillo de Tou sections (1083 m, Figs. 4, 6 and 7) correlated on the field by marker units and orthoimages. Stratigraphic thicknesses of the sections were measured with a Jacob staff, and geometric calculations based on field dip and strike data when direct measurements were not possible. The identification of the different SGF systems is based on the geological maps of Pickering and Bayliss (2009) and Cornard and Pickering (2019).

3.1 Magnetostratigraphy

The three sections were sampled for magnetostratigraphy (Figs. 4, 6 and 7) with a resolution of ten meters in average for Labuerda and Forcaz sections and twenty meters in average for the Morillo de Tou section. Such a resolution coupled with a mean sediment accumulation rate of approximately 30 cm/kyr in the Ainsa basin (Heard and Pickering, 2008) allows to capture all polarity reversals present in the time span of interest. Paleomagnetic core samples were drilled in fresh mudstone rocks focusing on the finest and less deformed marlstones. Thermal and few additional alternating field progressive demagnetization techniques were carried out on the samples at the Paleomagnetic Laboratory of Barcelona (CCiTUB- ICTJA CSIC; details about the methods can be found in *Supplementary material I, S.1.).*

3.2 Biostratigraphy

For biostratigraphy using nannoplanktons zones, approximately 200 grams of fresh rocks were collected in the finer (mudstones and siltstones) and less deformed lithologies in two sites of the Morillo de Tou section (Figs. 4 and 8; samples' GPS location in *Supplementary material I, S.3*).

3.3 Geochemistry

Approximately 200 grams of fresh material were collected per site targeting the finer (mudstones and siltstones) and less deformed lithologies at 30-40 cm below the weathering surface. A spacing of around 10 meters (stratigraphic depth) was applied between samples for each section. Oxygen and carbon stables isotopes ($\delta^{13}C$ and $\delta^{18}O$ values, both expressed in ‰ relative to VPDB standard) were measured in whole-rock carbonates (*Supplementary material I, S.1.2.5*). Major and trace elements (X-ray fluorescence, *Supplementary material I, S.1.2.2*), mineralogy (X-ray diffraction techniques, *Supplementary material I, S.1.2.3*) and the organic matter content (Rock-Eval) were determined on whole-rock material. Geochemical analyses were performed at the University of Lausanne (*Supplementary material I, S.1.2.4).*

4. Results

4.1 Stratigraphy

The stratigraphic succession sampled is composed of gray to dark massive or laminated hemipelagic marlstones alternating with turbiditic sandstones whose thickness vary between centimetric to metric scale. The fine-grained sediments show evidences of (1) slides/ slumps cohesive-flow deposits of metric scale, (2) typical abyssal zone ichnofossils (Nereites ichnofacies) (3) nummulitic packstones beds of centrimetric scale interpreted as tempestites (Cantalejo and Pickering, 2014) and (4) dark levels enriched in organic matter. Major SGF systems are characterized by debris flow deposits, erosive sandy channels and overbank hemipelagic deposits. These major clastic pulses of coarse sediments often show fining-upwards sequences. Off-axis deposits are characterized by marlstones dominant intervals.

4.1.1 Labuerda section

The Labuerda section (LB, Fig. 4) begins near the village of Labuerda. It has a stratigraphic thickness of 1000 m. This section begins in the Gerbe system and ends in the off-axis deposits of the Ainsa II submarine fan (A-II in Figs. 4 and 6). The lower part of this section is marked by an unconformity related to the emplacement of a thrust (Fig. 4). The interval above this thrust is composed of very fine marlstones interrupted by heterolithic intervals at approximately 400 m. Based on the map of Pickering and Bayliss (2009), we interpret this marlstone interval as the lateral equivalent of the Banaston SGF (Fig. 4). Due to the paucity of sandy beds in the sampled section, uncertainty is high in the identification of the second member (BII) of the Banaston SGF lateral deposits. This member is therefore indicated with a question mark in this study (B-II?, Fig. 6). At 879.5 m, the section reaches Ainsa I SGF sandbodies (A-I in Figs. 4 and 6). The Labuerda section eventually ends in the overbank deposits of Ainsa II (AII, Fig. 6). Slumps are present at the base and in the upper part of the section. The Labuerda section is marked by two darker beds around 210 m and 920 m and a nummulitic bed around 970 m (Fig. 6).

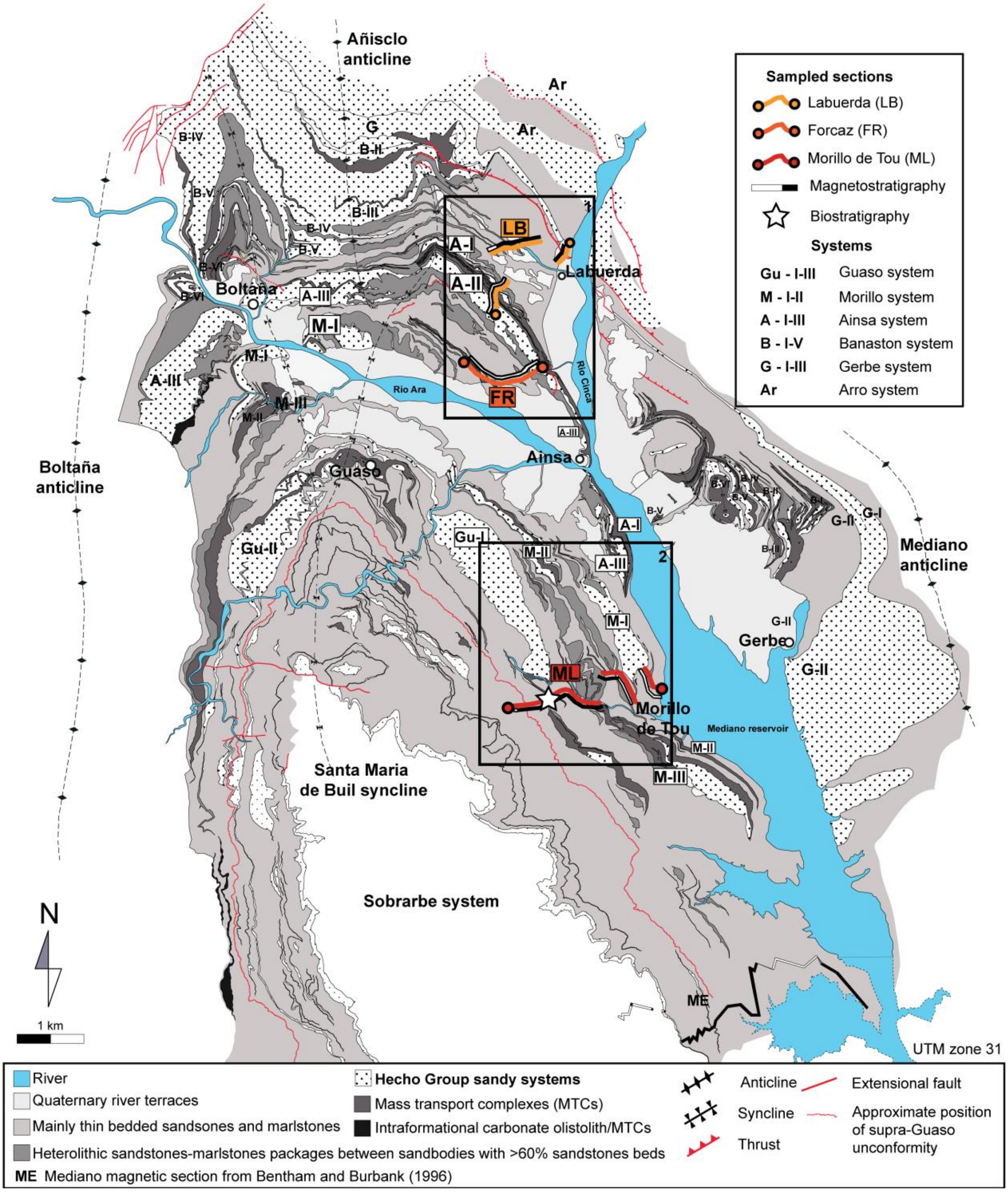

Figure 4. Geological map of the studied area redrawn from Pickering and Bayliss (2009) and Cornard and Pickering (2019). The sections sampled for magnetostratigraphy and geochemical analyses are indicated on the map (Labuerda, Forcaz and Morillo de Tou sections). Mediano magnetic section (ME) of Bentham and Burbank (1996) approximate position is also indicated. The studied successions are located on the eastern flank of the Santa Maria de Buil syncline which is also the western flank of the Mediano anticline.

4.1.2 Forcaz section

The Forcaz section (FR, Fig. 4) localized near the Forcaz stream begins at the base of Ainsa II SGF (A-II, Fig. 4). It overlaps Labuerda section (LB) with LB102 sample (Labuerda section) correlated to FR001 sample (Forcaz section, based on a lateral mapping of strata). This section of 462 m thickness begins at the base of Ainsa II SGF sandy package. A fining-upward sequence is observable at the top of Ainsa II sandbodies followed by a hemipelagic dominant interval of approximately 200 m in stratigraphic thickness (from 78 m to 287.5 m, Forcaz section, Fig. 6). At the top of Forcaz section, heterolithic beds are interpreted as belonging to Morillo I overbanks deposits (M-I, map Figs. 4 and Fig. 6). Two darker levels mark the Forcaz section at approximately 200 m and 260 m and a nummulitic bed occurs around 340 m (Fig. 6).

4.1.3 Morillo de Tou section

The Morillo de Tou section (ML, Fig. 4) begins near the namesake village, 6.5 km far from the former Forcaz section, and has a thickness of 1129 m. It begins in the marly interval between Ainsa and Morillo SGF systems. Correlation with the Forcaz section based on orthoimages places the base of the Morillo de Tou section approximately 10 meters above the top of the Forcaz section, which is corroborated later in this paper by the consistency of isotopic values across both sections. The Morillo de Tou section crosses Morillo I sandbodies (M-I, Fig. 4), rich in large forms of benthic foraminifers and various bioclasts, Morillo II-III (M-II, M-III) and Guaso I-II (G-I, G-II) overbank deposits (Fig. 7). Three intervals are notable in this section. First, an interval of massive marlstones of approximately 40 m is found between 720 and 760 m (Figs. 7 and 9). It is punctually characterized by centimetric scale darker beds (~10 cm and ~60 cm thick) and follows a large interval of slumped deposits and downlapping strata (Fig. 5C). Second, at 825 m, the so-called Castellazo level (Dreyer et al., 1999) consists of a carbonate breccia with meter-scale olistolithic blocks of bioconstructed carbonates (Fig. 5B), interpreted as collapsed from fringing limestone formations (Dreyer et al., 1999; Mochales et al., 2012a). A similar level with smaller blocks is observed around 620 m (Fig. 7). Third, the so-called San Lino level is a thick (about 1 m), regional level of dark mudstones (Fig. 5A) identified in Dreyer et al. (1999), and interpreted as a marker of a basin-wide episode of anoxia by Mochales et al. (2012a). It also corresponds to a dark shale horizon and sample MFS-4 in Scotchman et al. (2015). This level is considered as the base of the overlying Sobrarbe deltaic complex (Arbués et al., 2011). Finally, the Morillo de Tou section is characterized by a nummulitic bed at 100 m (Fig. 7) and few dark mudstone levels around 440 m and 970 m (Fig. 7).

4.2 Magnetostratigraphy and biostratigraphy

The marlstones of the Ainsa basin show a viscous component below 280°C. Above this temperature, a Characteristic Remanent Magnetization (ChRM) component is isolated for most of the samples. The maximum unblocking temperature of the ChRM is observable from 400º to 450°C in the most stable samples (See *Supplementary material I,* Fig. S.2.1). This range of temperature suggests that iron oxides such as magnetite are the main magnetic carriers. Previous paleomagnetic studies (Muñoz et al., 2013; Mochales et al., 2012a) highlighted a rotation of the Ainsa basin clockwise up to 60°. A north-east direction with downwards inclinations is thus expected for normal polarity samples, and south-west directions with upwards inclinations is expected for reverse polarity samples (See *Supplementary material I,* Fig.S.2.1). The significant clockwise rotation recorded by normal and reversed polarity ChRM components makes them easily distinguishable from north-directed recent overprints. Samples showing unexpected orientations are indicated in white in Figures 6 and 7 and were not considered to define normal/reverse polarity magnetozones in the local magnetostratigraphy. For sites where multiple samples were measured, the specimen showing the best quality was selected

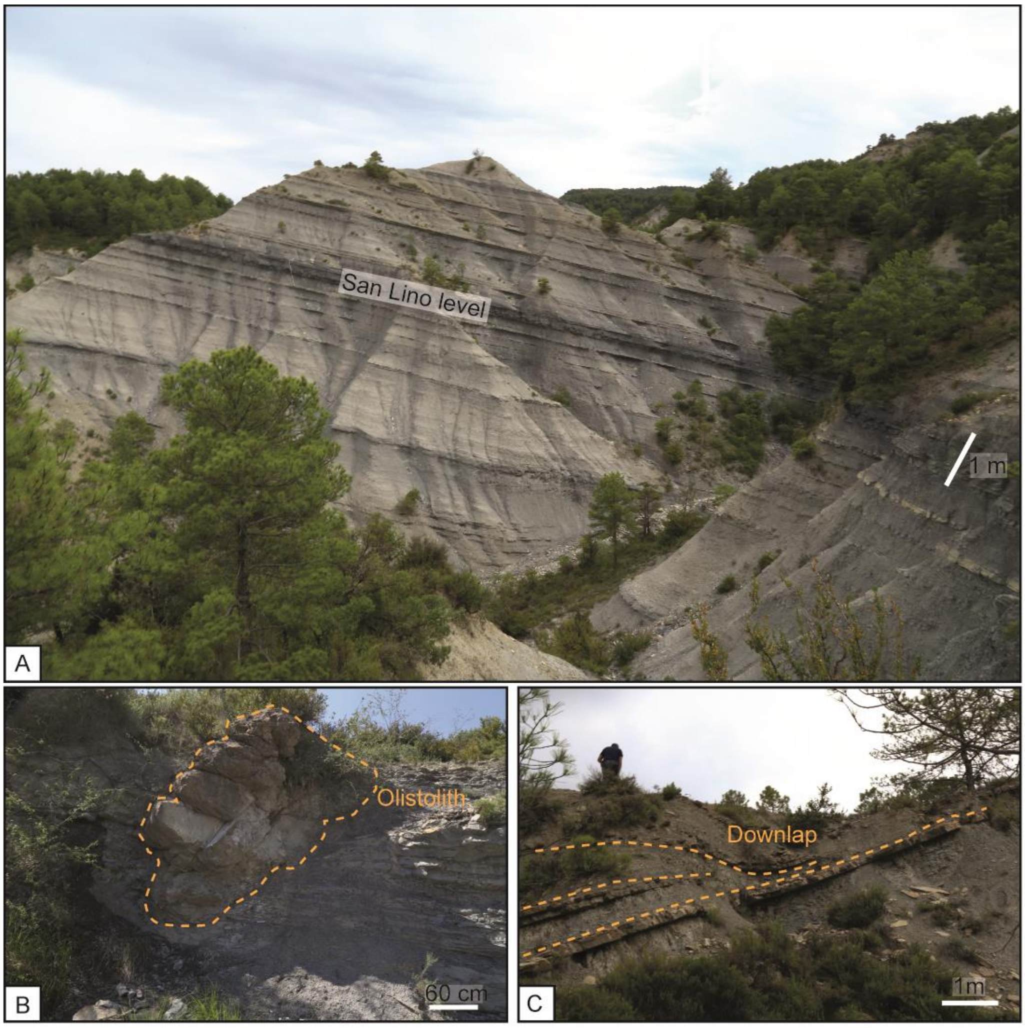

Figure 5. Interpreted field photographs from Morillo de Tou section (A) San Lino level with typical alternance of marlstones and isolated sandy beds. (B) Olistolith from the Castellazo level (bioconstructed limestone) (C) Dowlap geometry on erosive surface suggesting slump scar.

for VGP (Virtual Geomagnetic Pole) calculation. Samples with magnetic moment non-conform to the expected Eocene magnetic paleofield represent approximatively 45 % of the results. They are distributed on all the three sections with a cluster between LB009 and LB035 at the base of Labuerda section and one at the top of Morillo de Tou section (MT35 to MT43 samples). Several causes may account for samples showing flawed directions. At the base of Labuerda section, our cluster of flawed directions could be explained by slumps or tectonic deformations associated to minor splays from the neighbouring thrust. The second cluster of flawed directions is again associated with a large interval characterized by slumps (650-700 m in the Morillo section). Another source of error is the application of an external high field generated, for instance, by a lightning strike, which will produce magnetic moment with intensity orders of magnitude higher than regular samples (LB013-LB014). Finally, samples close to reversal boundaries can also show unusual directions due to either the distinct non-dipolar behavior of the Earth’s magnetic field during transitions and/or the delayed locking and overprint of both normal and reverse components upon burial (e.g. LB058 to LB061, Fig. 6). Few samples also punctually show unexplained and unexpected directions and were rejected (LB017-1B, LB024-1B, LB033-1C, LB035-2A and B, LB037-1B, LB054-1B, LB055-1A, LB057-1B, LB059-1B, LB085.2A, LB109-2A and FR20-2A). In total, 35 samples of quality one, 39 samples of quality two and 5 samples of quality three give a reliable record of the different magnetozones occurring in the basin.

The Labuerda magnetic section begins with a clear normal polarity zone (N1, LB003-LB008, Fig.6) followed, from LB009 to LB035, by a cluster of noisy data. From LB035 to LB059, normal polarity is again measured (N2, Fig. 6). At LB060 (528 m, Fig. 6), a clear reversal from normal polarity zone (N2) to reverse polarity zone (R1) occurs. From LB060 (528 m) to FR040, almost all samples indicate reverse polarity (R1, Fig. 6). As Forcaz and Labuerda sections are overlapping, the reversal magnetozone identified in both sections corresponds to R1 (Fig. 6).

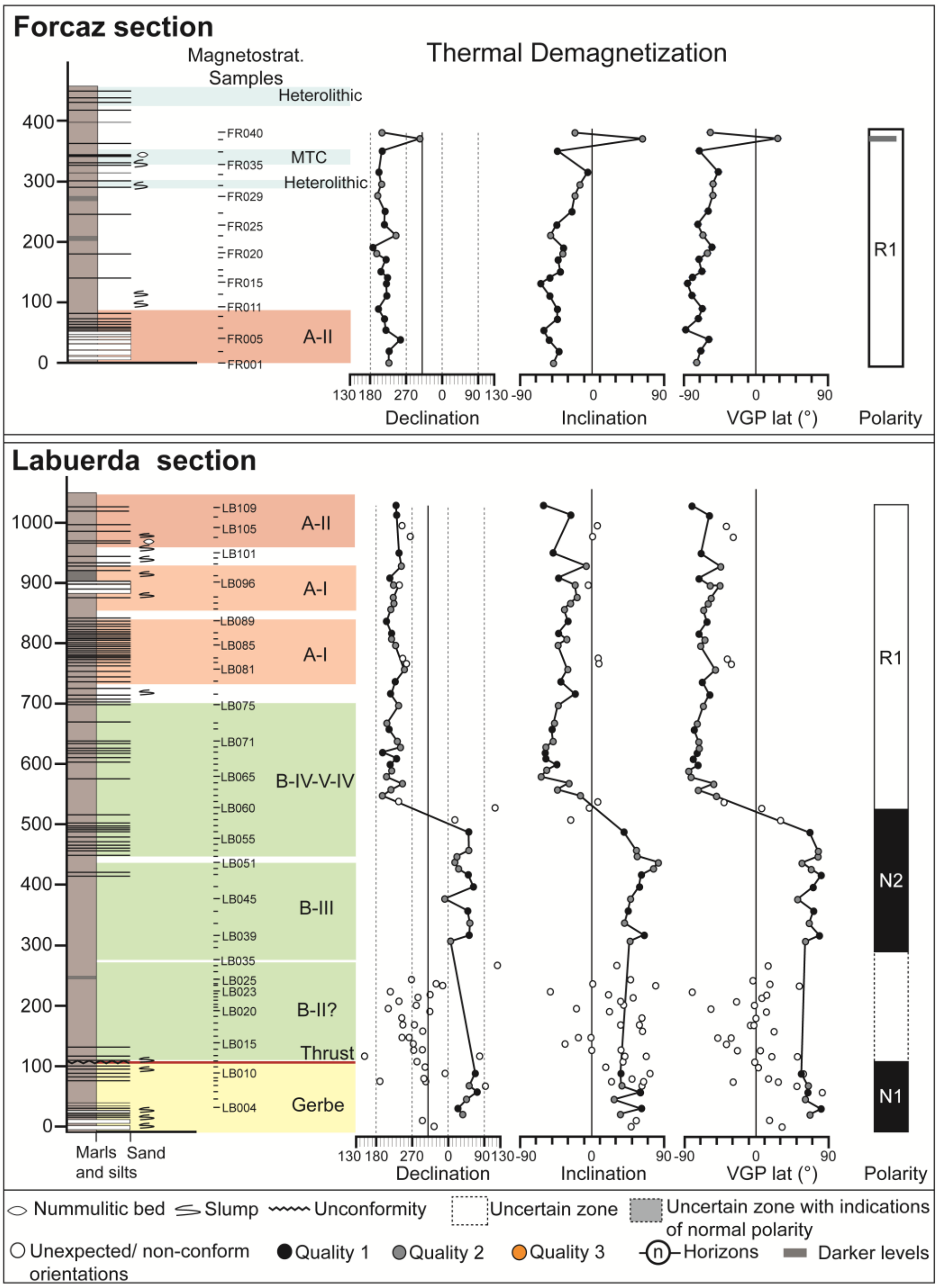

Figure 6. Stratigraphic column (on the left) and magnetostratigraphic data by thermal demagnetization (on the right) for Labuerda and Forcaz sections (localization Fig. 4). In the Labuerda section, samples above 300 meters are neatly aligned and separated in two different polarity zones. In the segment between ~100 and 300 m it remains difficult to interpret the paleomagnetic signal unambiguously possibly due to the presence of minor splays from the main thrust mapped by Pickering and Bayliss (2009). In the Forcaz section, only the uppermost before-last sample indicates a normal polarity and it is thus represented as a grey level in the R1 chron. Abbreviations: B: Banaston SGF; A: Ainsa SGF; MTC: mass transport complexes.

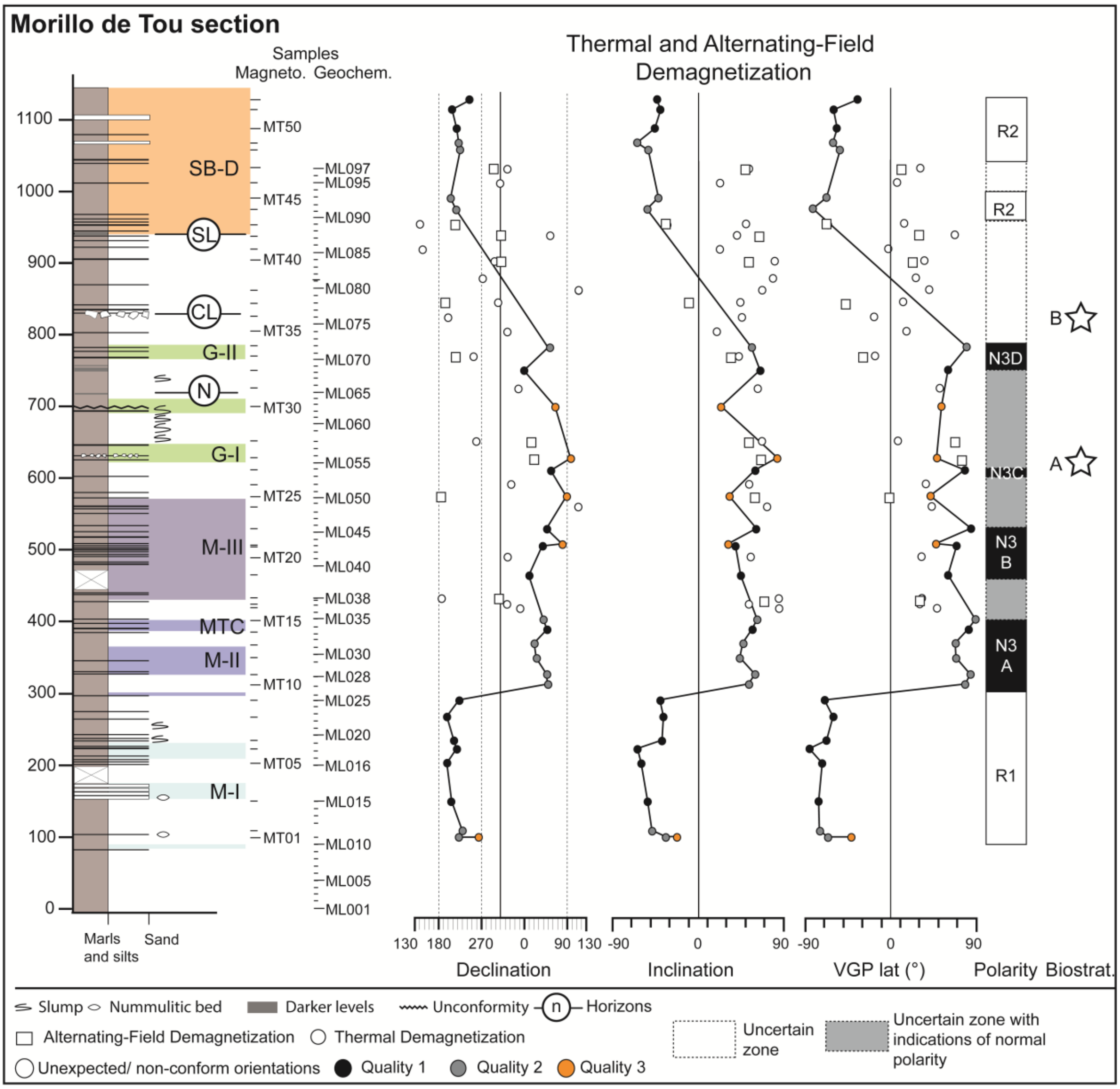

Figure 7. Stratigraphic column (left) and magnetostratigraphic data (thermal demagnetization and Alternating-field demagnetization) for the Morillo de Tou section (location Fig. 8). Note the clear reversal from reverse (R1) to normal (N3A) polarity at ca. 300 m followed by a large number of unclear and low-quality data from 400 m to 976 m. Samples indicate reverse polarity for the top of the section. From N3A to N3D, despite ambiguous declination, inclination is always positive suggesting normal polarity. Note the low quality of the alternating field data and ambiguous orientations and the position of two biostratigraphic sites (stars A and B). Abbreviations: SL: San Lino level; CL: Castelazzo level; N: Negative oxygen excursion level; MTC: Mass transport complexes; N: normal polarity; R: reverse polarity; M: Morillo SGF; G: Guaso SGF; SB-D: Sobrarbe deltaic complex.

The quality of magnetostratigraphic samples for the Morillo de Tou section (MT, Fig. 7) is lower than for the Labuerda and Forcaz sections. Clear magnetozones can still be identified but the larger proportion of noisy samples lead to uncertainties in the exact position of the magnetic polarity reversals. The magnetostratigraphic dataset begins 100 m above the geochemical dataset of the Morillo de Tou section (ML section) with a clear reverse interval (MT01-MT09, R1, Fig. 7). At MT10 (313 m), a polarity reversal is recorded. The following normal polarity (MT10-MT33, Fig. 7) is subdivided in three normal polarity zones N3A, N3B and N3C due to the unexpected declinations measured in the samples (Fig.7). Despite these unexpected declinations, inclinations remain positive indicating a normal polarity magnetozone. From MT35 to MT47, measured samples show mixed declinations and inclinations. From MT48 to MT52, a clear reverse polarity is recorded (R2, Fig. 7). The geographical localization of the samples as well as their polarity (normal, reverse and unclear) are reported in Figure 8.

Alternating-field method (AF, squared dots Fig. 7) was additionally performed on ten cores of the Morillo de Tou section. The samples provide low quality results (50% of quality 3 samples) with numerous unexpected orientations among quality 1 and 2 samples. Due to the low resolution between samples and the low quality of the data, AF results were not used further in this study.

Fisher means were calculated for all reliable reverse and normal samples (See *Supplementary material I, Fig.S.2.2*). After tilt correction, a mean declination/inclination of 44.4°/53.4° for the normal polarity and 221.3°/-39.7° for the reverse polarity intervals were obtained from all the reliable samples. Those results are consistent with the measured clockwise rotation of the basin (Muñoz et al., 2013). Finally, paleomagnetic means in stratigraphic (tilt corrected) coordinates are better clustered than in geographic coordinates which support a pre-folding ChRM acquisition (See *Supplementary material I, Fig.S.2.2*).

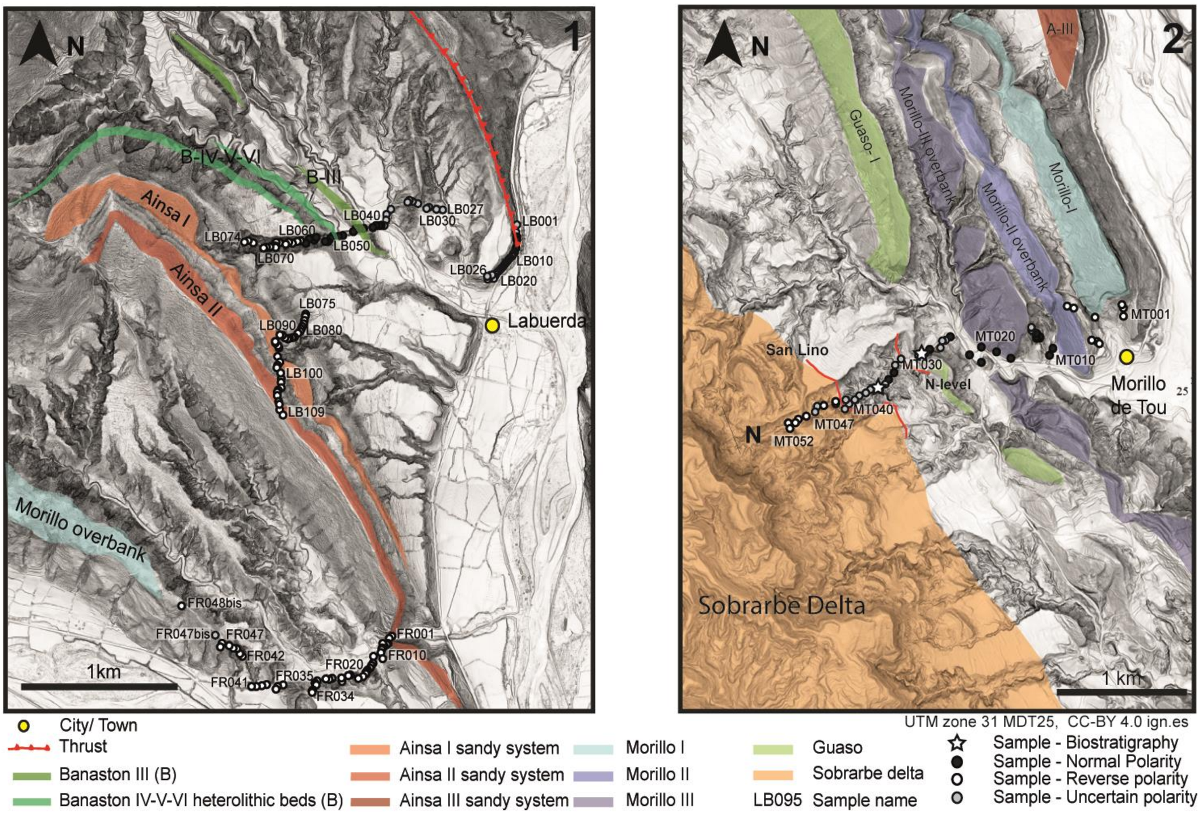

Figure 8. Detailed magnetostratigraphic sections on high-resolution (LIDAR) digital elevation models (Fig. 4 for area 1 and 2 localizations). Sandy packages of sediment gravity flow systems are indicated in color based on the geological map of Pickering and Bayliss (2009). Black dots indicate a normal polarity zone, white dots indicate reverse polarity. The position of the San Lino level interval as indicated in Mochales et al., (2012a) and the negative oxygen excursion (N-level, section 4.3.1.1) are also indicated. (Digital elevation model from the Centro nacional de Informacion Geografica, PNOA, 264-4706; https://centrodedescargas.cnig.es, MDT25 2015 CC-BY 4.0 ign.es)

The two analyzed biostratigraphic sites, (sample A: ML055 and B: ML075) are indicated in Figure 7. Sample (A) bears the following nannofossils: *C. expansus, S. furcatolithoides, S. spiniger, R. hillae, R. umbilicus, S. runus, D. wemmelensis, C. vanheckiae, S. obtusus, S. richteri, D. filewiczii*, and *D. stavensis*. They are ascribed to lowermost NP16 zone (Eocene-Lutetian). In sample (B) the nannofossils *D. bifax, S. furcatolithoides, S. spiniger, C. vanheckiae, C. solitus, R. umbilicus, S. runus*, and *S. richteri* indicate early NP16 zone (Eocene-Lutetian). For the detailed nannopalaeontology, refer to the *Supplementary material I, S.3*.

4.3 Geochemistry

4.3.1 Stable isotopes

The main source of uncertainty of isotope records in sedimentary archives is the alteration of the primary signal, mainly caused by diagenetic processes. In the Ainsa basin, while the values are significantly lower than their global equivalents, the isotope trends are considered as being preserved for both carbon and oxygen isotopes as (1) no covariation (R = 0.2658) was observed between $\delta^{13}C$ and $\delta^{18}O$ values (Castelltort et al., 2017, and this study data), and (2) both $\delta^{13}C$ and $\delta^{18}O$ profiles mimic global curves (e.g., Cramer et al., 2009). The shift of the absolute $\delta^{13}C$ and $\delta^{18}O$ values is possibly due to burial (e.g., Irwin et al., 1977) and the restricted physiography and proximal position of the basin (Castelltort et al., 2017).

4.3.1.1 Oxygen stable isotope

Oxygen isotope data varied between -6 and -4 ‰ in the studied succession Fig. 9). In Labuerda and Forcaz sections, the $\delta^{18}O$ values show a linear trend toward progressively higher values (LB001 to FR047, Fig. 9). The lower part of Morillo de Tou section shows a small decrease in $\delta^{18}O$ values succeeded by approximately 600 m of a sediment pile with $\delta^{18}O$ around -5 ‰. This stable interval is interrupted by a negative excursion at 720.5 m (-6.97 ± 0.07‰ $\delta^{18}O$, ML065, N-level, Fig. 9). After this negative oxygen isotope excursion (N-level), $\delta^{18}O$ returns to pre-excursion values and progressively becomes more positive.

4.3.1.2 Carbon stable isotope

The carbon isotope records show large-scale positive and negative shifts in all sections (Fig. 9). At the base of the studied section, the Gerbe system is characterized by negative values showing small-scale variations of the $\delta^{13}C$ around -1.5 ‰ (see Gerbe in Fig. 9), which is consistent with data in Castelltort et al. (2017). Banaston SGF system is marked by a positive excursion of the $\delta^{13}C$ values (from -0.8‰ to 0.4 ‰ in B-II? member, Fig. 9) also noticed by Castelltort et al. (2017). More negative $\delta^{13}C$ values were measured on the succession covering Banaston's off axis deposits (B-III-IV-V-VI) and Ainsa (I-II) SGF systems (Fig. 9). Above the Ainsa II sandy deposits (A-II in Fig. 9), starts a progressive shift to higher $\delta^{13}C$ values, which is mostly associated with marlstones deposits.

From Forcaz to Morillo de Tou sections, the $\delta^{13}C$ profiles show more positive values with small-scale variations between -1 and 0 ‰ near Morillo I sandbodies and Guaso II SGF packages (Fig. 9).

4.3.2 Organic matter analysis

The total organic carbon content (TOC in wt.%) in the marlstones of the Ainsa basin are generally low (0.26 wt.% on average; Fig. 9). Two distinct trends can be noted in the studied succession. From Gerbe to Ainsa II, TOC concentrations are averaging around 0.24 wt.% (LB001 to FR027, Fig. 9) while from Ainsa-II (FR028) to the Sobrarbe deltaic complex (ML096), TOC concentrations average 0.32 wt.%. This general pattern is punctuated by few discrete increases in the TOC concentrations in the Gerbe SGF package (Gerbe, Fig. 9), the Ainsa II SGF package (TOC values up to 0.49 wt.%, A-II, Fig. 9) and in the Forcaz section (FR030 to FR047, Fig. 9).

The few darker levels identified in the basin are not correlated with a substantial increase in the TOC (e.g., San Lino level in the Morillo de Tou section, SL, Fig. 9), except for a darker marlstone interval in the Guaso SGF system (N-level in the Morillo de Tou section, 720.5 m, Fig. 9). This level is characterized by a significant increase in TOC up to 0.70 wt.%) and coeval with a strong negative excursion of the $\delta^{18}O$ values (-6.97 ± 0.07‰, Fig. 9).

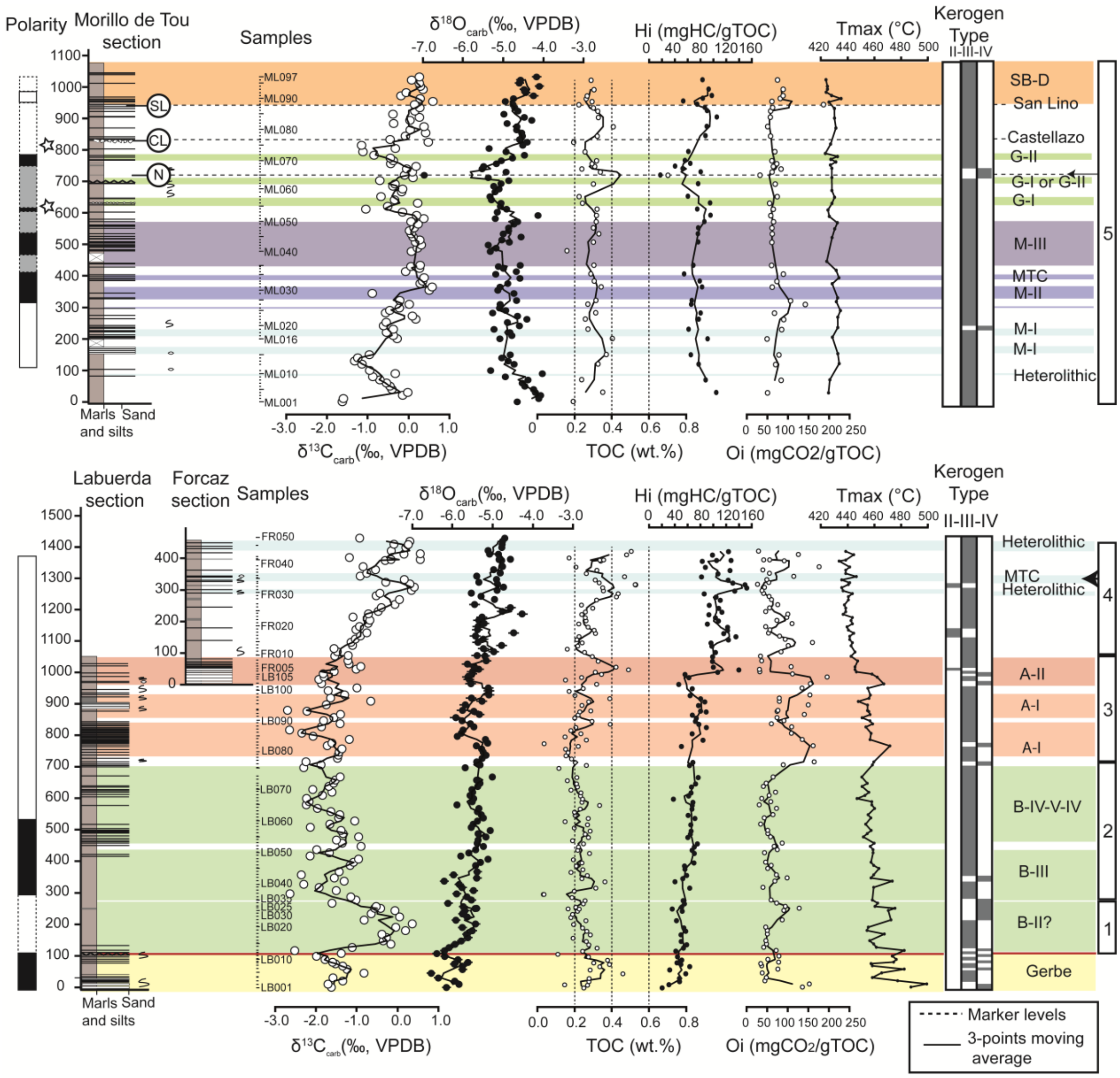

Figure 9. Isotopic and Rock-Eval results (Labuerda, Forcaz and Morillo de Tou sections) Note the negative excursion of oxygen isotope at 720.5 m. Hi, Oi and Tmax are plotted for TOC > 0.2 wt. %, stars indicate the position of biostratigraphic sites and numbers on the right refer to points mentioned in sec. 5.2.2. Standard deviations on measurements are indicated by horizontal bars. Abbreviations: SL: San Lino level; CL: Castelazzo level; N: Negative oxygen excursion level; MTC: Mass transport complexes; B: Banaston SGF; A: Ainsa SGF; M: Morillo SGF; G: Guaso SGF; SB-D: Sobrarbe deltaic complex.

The ratio of HI (hydrogen index) versus OI (oxygen index) and HI versus T_{max} (maximum temperature), for TOC higher than 0.2 wt. %, inform about the type of kerogen (II-III or IV) found in the basin and the different source of organic matter (McCarthy et al., 2011, Fig. 10). Type II kerogen is sourced from plankton and algae in marine settings, type III kerogen has an important contribution of terrestrial plant derived organic matter deposited in marine environments and type IV kerogen correspond to eroded, reworked or biologically oxidized organic matter (McCarthy et al., 2011). For the upper Hecho Group, HI-OI and HI-T_{max} plots suggest that the organic matter is principally type III kerogen with few samples within the fields of type II and IV kerogens (Figs. 9 and 10). The predominant continental input of organic matter in the Ainsa basin is punctually replaced by marine organic matter (kerogen II) and reworked, oxidized and eroded organic matter (kerogen IV). An increase in HI can be noted in the Forcaz section coupled with the occurrence of type II kerogen (Fig. 9 and FR samples in Fig. 10B). Most of type IV kerogen samples are clustering at the base of the studied section (see Gerbe, B-II? And B-III members in Fig. 9). During Guaso SGF systems deposition, a decrease in HI values indicates a pronounced input of terrestrial organic matter coeval with the negative $\delta^{18}O$ excursion.

Finally, the general increase of T_{max} with depth and the general shift from immature to overmature organic matter in the basin with increasing depth (LB, FR and ML clusters in Fig. 10B) reflects the increasing thermal maturation with burial (Fig. 9).

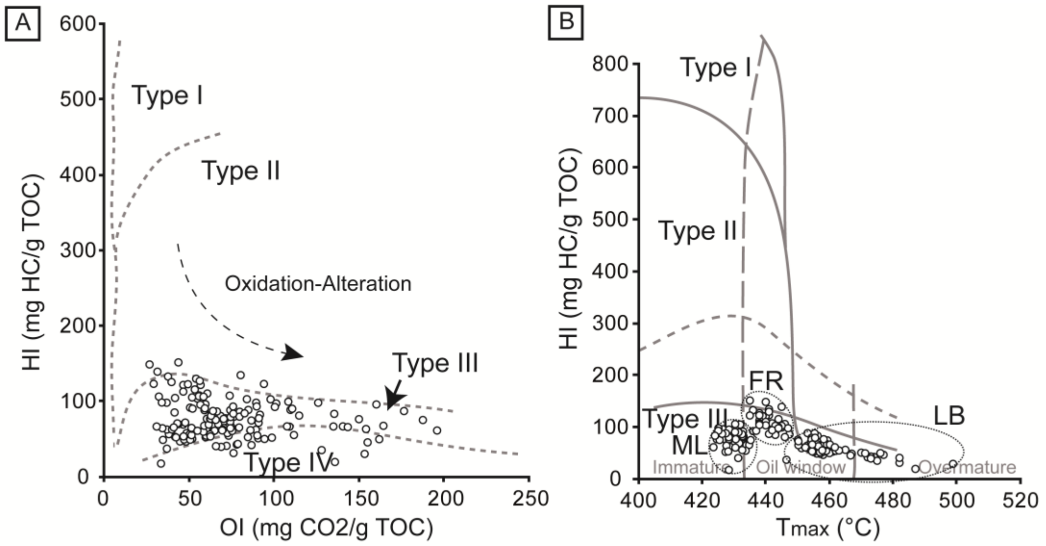

Figure 10. HI vs OI (A) and HI vs Tmax (B). Organic matter is generally type III and IV kerogen which indicates plants from terrestrial setting source or biological alteration of the organic matter (McCarthy et al., 2011). Abbreviations: LB: Labuerda section; FR: Forcaz section; ML: Morillo de Tou section.

4.3.4 Mineralogy, major elements and trace elements

X-ray fluorescence and X-ray diffraction data for Labuerda and Forcaz sections can be found in the *Supplementary Material I, S.4*. This dataset, acquired at low resolution, allows the identification of the main sequences of fining and coarsening upward and supports the main stratigraphic interpretation (See *Supplementary Material I, S.4*). Due to the absence of a record for the Morillo de Tou section and the low resolution of our data, these results are not discussed further in this text.

4.3.5 Ainsa stack

The compilation of Castelltort et al., (2017) and this study data generates an isotopic and geochemical dataset for the complete Hecho Group in the Ainsa basin (Fig. 11). Correlation between the Pueyo off-axis section (Castelltort et al., 2017, Fig. 11) and the Labuerda section (this study) was assessed with geological map and supported by lateral isotopic records correlation (LB021=GB33, in B-II?, Fig. 11). In this work, Banaston I was placed in the turbidite stack previously identified as Gerbe II by Castelltort et al., 2017. Our interpretation is in accordance with the map of Cornard and Pickering (2019) and set the correlation between both section in the lateral equivalents of Banaston I (Fig. 11).

A geochemical dataset (carbon and oxygen stable isotopes, TOC, HI, OI and T_{max}) of 3767 m (stratigraphic thickness) covers the entire Hecho Group (from Arro SGF system to the distal deposits of the Sobrarbe deltaic complex, Fig. 11). High amplitude shift of $\delta^{13}C$ ratio can be noted along the basin's studied succession with generally high values for Morillo, Guaso SGF systems and the distal deposits of the Sobrarbe deltaic complex (Fig. 11). The $\delta^{18}O$ values show a gradual increase toward the top of the basin, interrupted by a negative excursion at 3455 m (ML065, Morillo de Tou section, N-level; Figs.

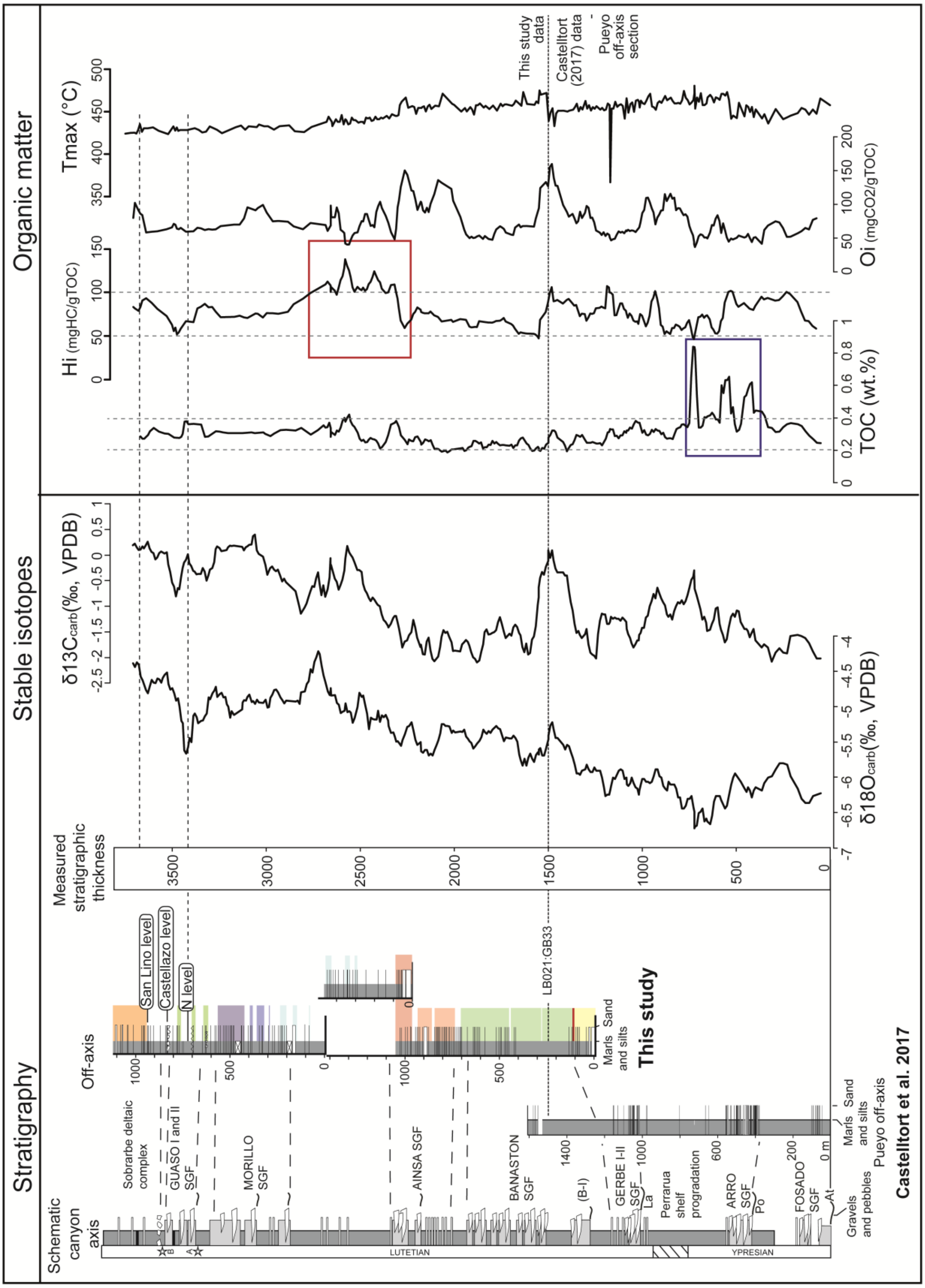

Figure 11. Compilation of Castelltort et al. (2017) and this study datasets with 5-points moving average isotopic, total organic content, hydrogen index, oxygen index curves and Tmax (°C; raw data). The two new biostratigraphic samples (A and B) are indicated by stars in the Schematic canyon axis column. In δ^{18}O data, a clear negative excursion can be noted (N-level in the Guaso system).

9 and 11). The marlstones of the Ainsa basin have a TOC close to 0.3 wt.% except for a clear interval enriched at the base of Pueyo off-axis section (Fig. 11, blue rectangle in the Pueyo off-axis section). In

Figure 11, the positive TOC excursion observed during the N-level (N-level, sec. 4.3.2, Fig. 9) is buffered by the 5-points moving average. High Hi values can be observed in the marlstone interval succeeding Ainsa SGF sandy packages (red rectangle, Fig. 11) suggesting major pulses of marine organic matter.

5. Discussion

The cyclicity of sediment gravity flow deposits of the Ainsa basin has been studied by several authors (e.g., Pickering and Bayliss, 2009; Cantalejo and Pickering, 2014; Scotchman et al., 2015; Castelltort et al., 2017; Clark et al., 2017). These studies converge towards the conclusion that, while local tectonics did control the large-scale geometry of the deposits (Vinyoles et al., 2020), cyclic stratigraphy at multimillennial scale may rather be controlled by climatic modulations (Pickering and Bayliss, 2009). More specifically, Cantalejo and Pickering (2014, 2015) recognized Milankovitch type cyclicities with elemental and isotopic composition of several sections of the Ainsa basin. They suggested a control of Milankovitch driven climatic cycle on sediment export through change in humidity or small scale eustatic variations directly related to climate (Cantalejo and Pickering, 2014). The geochemical dataset of Scotchman et al. (2015), in the Guaso system, also highlighted a dominant orbital component in the frequency of terrigenous input in the Ainsa basin. Recently, $\delta^{13}C$ variations in the lower part of the succession (Fosado to the lower Banaston systems tied to the eustatic curve of Miller et al. (2005), seem to indicate a dominant, but not exclusive, eustatic control on the occurrence of SGF packages in the basin (Castelltort et al., 2017). A robust chronostratigraphy of the successions is crucial to decipher the possible drivers behind such sedimentary signals. Previous age constraints in the Ainsa basin are provided by the magnetostratigraphic studies of Holl and Anastasio (1993), Bentham and Burbank (1996), Mochales et al. (2012a) and Cantalejo et al. (2020), the biostratigraphic data of Jones et al. (2005), Pickering and Corregidor (2005) and Scotchman et al. (2015), as well as by the carbon isotope stratigraphy of Castelltort et al. (2017). In this paper, our high-resolution magnetostratigraphic dataset provides material to build a precise age model from Banaston SGF system to the Sobrarbe deltaic complex.

5.1 New age model for the upper Hecho group

The age model developed in this study is based on a new magnetostratigraphic dataset integrated in the frame of earlier magnetostratigraphic studies of Mochales et al. (2012a), Bentham and Burbank (1996) and Cantalejo et al. (2020). This age model is strengthened by existing and new biostratigraphic data. Correlations with existing studies are based on the lateral and vertical continuity of the sedimentary series observed in the Ainsa basin. This suggests the absence of major hiatuses, unconformities and a preservation of all magnetozones.

The total composite magnetostratigraphic section consists of five long magnetozones (Fig. 6, 7 and 12) correlated to the existing stratigraphic divisions of the Ainsa basin by regional marker levels. The studied series begin with the normal polarity N1 in the Gerbe system followed by a normal polarity for the lower systems of Banaston (N2, Fig. 12). A shift to reverse polarity (R1) is observed up to Morillo SFG system where polarity shifts back to normal (N3 A, B, C and D, Fig. 12). The distal deposits of the Sobrarbe deltaic complex are characterized by a reverse polarity (R2, Fig. 12). The correlation with Mochales et al. (2012a) is done by the identification of the San Lino regional marker level in N3 (Figs. 5, 7, 9 and 13). In Mochales et al. (2012a), this dark level is located 20 meters below the C20n to C19r boundary (*ca.* 42.4 Ma recalibrated to GPTS 2012) which suggest that N3 correspond to C20n and R2 to C19r. Interpretation of N3 A, B, C and D as belonging to the same normal interval is

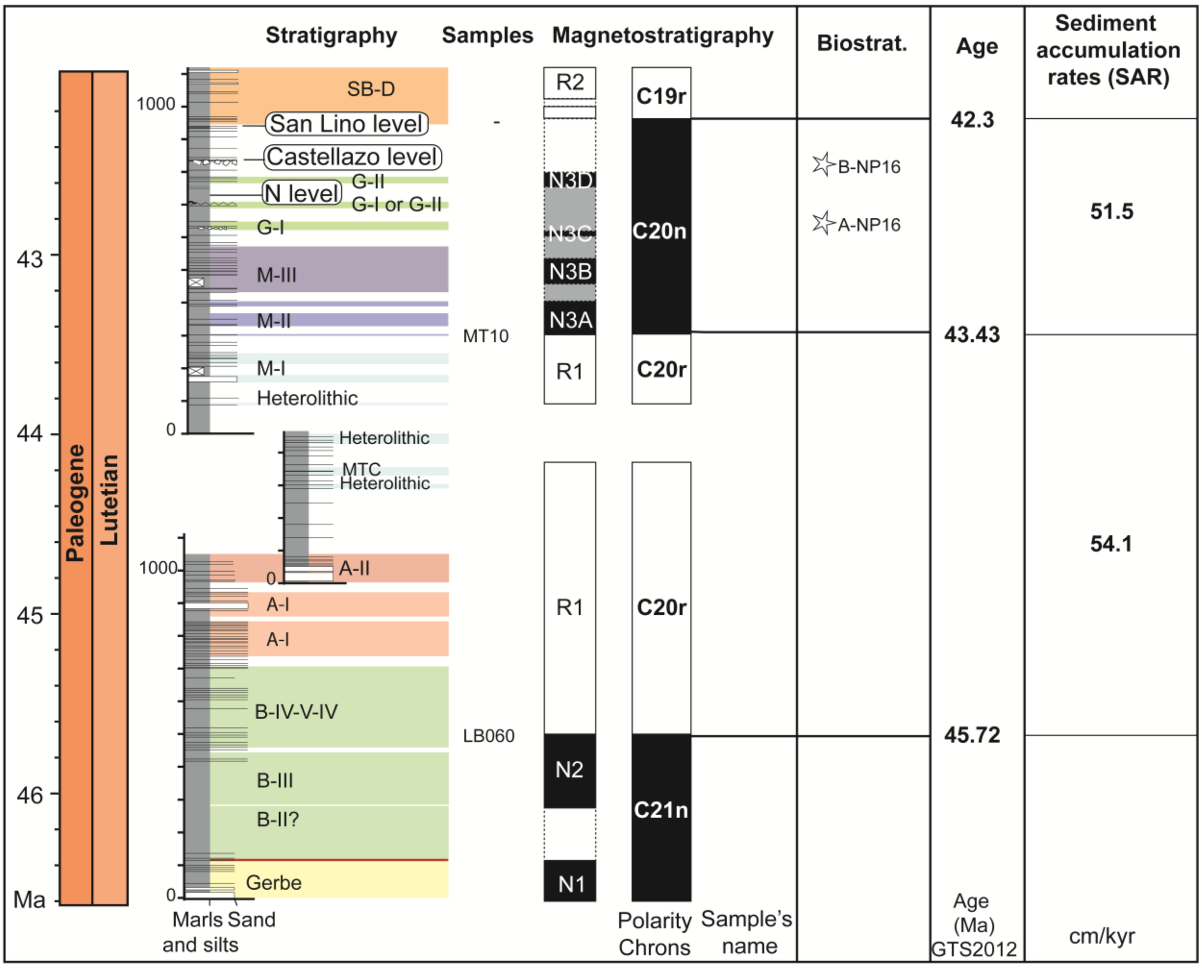

Figure 12. Interpretation of magnetozones by correlation to the GPTS. Note the two biostratigraphic samples (A) and (B) indicated by stars in the Morillo de Tou section. Data has been plotted using Time Scale Creator 6.8 (Ogg and Lugowski, 2020, with the 2012 GPTS; Gradstein et al., 2012). Abbreviations can be found in Fig. 9.

consistent with the data of Mochales et al. (2012a) that identified a long normal polarity zone below the San Lino level (Coscollar section, Fig. 13). This interpretation is also in concordance with the C20n chron identified bellow the Sobrarbe delta by Bentham and Burbank (1996; Mediano section, Fig. 13) and is coherent with the identification of NP16 nannoplankton zone in two new biostratigraphic sites in the Guaso SGF system (ML065 (A) and ML075 (B) in Fig. 12). The exact position of the reversal between C20 and C19 chrons is questionable in our section due to the paucity of good quality's data in this stratigraphic interval. It was however placed 20 meters above the San Lino level in accordance with Mochales et al. (2012a) dataset. In Mochales et al. (2012a) the identification of C19r was confirmed by two biostratigraphic data (GO and EO) indicating SBZ15 in the Coscollar section (Fig. 13).

Considering continuous sedimentary series, R1 is interpreted as C20r and N1 and N2 as C21n. The identification of C21n in the Banaston SGF system is supported by the presence of large benthic foraminifera and nannoplanktons characteristic of SBZ13 and NP14 respectively (Scotchman et al., 2015). The N1 normal zone is identified as belonging to the C21n chron in accordance with Castelltort et al. (2017) age model. This interpretation is consistent with Cantalejo et al. (2020) age model based on magnetostratigraphy acquired in different sections in the basin. Both models have slight differences regarding the exact position of two reversals found in the succession of the upper Hecho Group. First, Cantalejo et al. (2020) place more precisely the transition from C21n to C20r between BV and BIV and secondly, the transition from C20r to C20n is placed before the second member of Morillo (M-II) in this study while Cantalejo et al. (2020) place it during M-III member. As seen in Figure 13, the sedimentary series are condensed near the Boltaña anticline (shorter Coscollar section of Mochales et al., 2012a) and on the eastern flank of the Mediano anticline (Bentham and Burbank, 1996; Fig. 13). According to this age model, the Hecho Group was deposited between 50.5-50.2 Ma (Castelltort et al., 2017) and ~42.3 Ma (this study). More precisely, the marlstones above Banaston III-IV SGF systems are dated at 45.72 Ma and the base of Morillo II at 43.43 Ma (GTS 2012; Gradstein et al., 2012; Fig. 12). Thus, crude sediment accumulation rates are estimated at (1) 54.1 cm/kyr between Banaston IV and Morillo II SGF, (2) 51.5 cm/kyr between Morillo II SGF deposits and the San Lino level (Fig. 12).

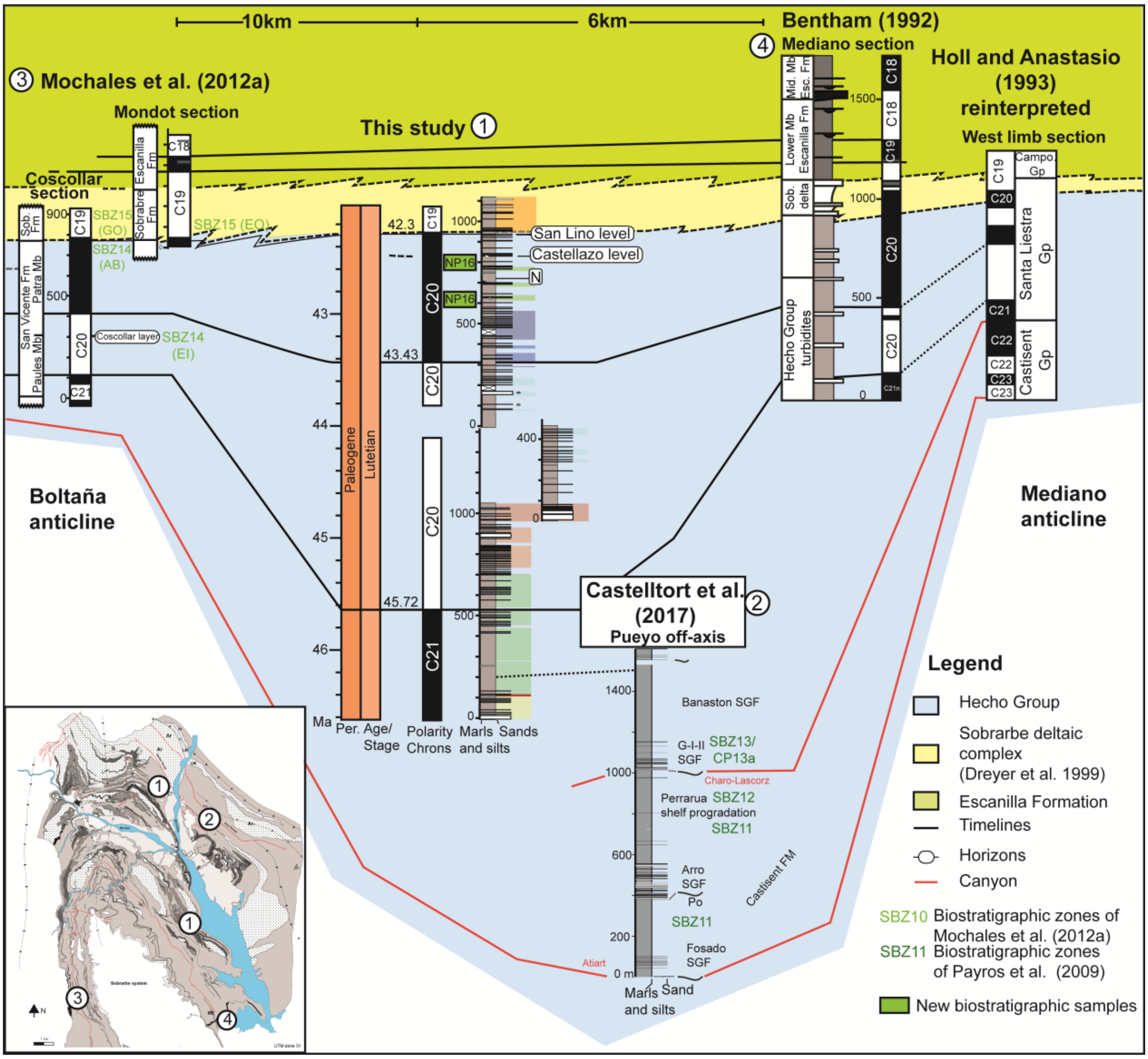

Figure 13. Principal correlations with the stratigraphic sections of Bentham (1992), Holl and Anastasio (1993), Mochales et al. (2012a) and Castelltort et al. (2017). Vertical thicknesses are respected. Note the important changes in stratigraphic thickness between this study and Mochales et al.(2012a) sections and the high preservation of the deep marine series in the Ainsa basin. Abbreviations can be found in Fig. 9.

5.2 Local isotope signal versus global records

The new age model based on magnetostratigraphy and biostratigraphy was used to tune the newly acquired isotopic dataset. The primary carbon and oxygen isotope composition of the whole-rock carbonates that precipitate in equilibrium with the dissolved inorganic carbon (DIC), reflects the isotopic signal of the surrounding oceanic water. Therefore, the $\delta^{13}C$ and $\delta^{18}O$ data were compared to global isotopic target curves (Cramer et al., 2009, recalibrated to GTS 2012, Gradstein et al., 2012, by Grossman, 2012) and eustatic global records (Miller et al., 2005; Kominz et al., 2008) in order to explore the origin of the isotopic signal and the possible relationship between stratigraphy and sea-level variations (Fig. 14).

5.2.1 Stable oxygen isotopes

Oxygen isotopes are well known to be a proxy for paleotemperatures (e.g. Lisiecki and Raymo, 2005). The middle Eocene climate is characterized by transient conditions from greenhouse to icehouse climate (e.g. Tripati et al., 2005) with indicator of development of Antarctic ice sheets (e.g., Pekar et al., 2005). During the deposition of the upper Hecho Group, the climate underwent a progressive cooling initiated after the Early Eocene Climate Optimum (EECO, ~49 Ma). This progressive cooling was interrupted by the global Middle Eocene Climatic Optimum event (MECO) subsequent to the deposition of the Hecho Group (*ca.* 40.5 Ma to 40 Ma; Sluijs et al., 2013; Westerhold and Röhl, 2013; Boscolo Galazzo et al., 2014). During the deposition of the Hecho Group, the general trend toward more positive $\delta^{18}O$ values (Fig. 14) suggests a gradual cooling that mirrors the global record. This progressive shift is solely interrupted by a negative excursion recorded in the Guaso SGF system, possibly reflecting a local warming event or a possible restriction of the connectivity in the basin and enhancing the influence of meteoric waters signal from the continent. At the million-year timescale, we think that the progressive coarsening-upward character of the stratigraphic record is to be linked primarily with the general basin filling sequence of the Pyrenean foreland basin rather than with the progressive cooling trend of the global climate. It is however important to note that, despite being deposited over an actively deforming template at the front of a growing orogen, this clastic deep-water succession preserves a quite faithful record of the global isotopic signal in oxygen.

5.2.2 Stable carbon isotopes

In the Pueyo off axis section of Castelltort et al. (2017; see plotted dataset in Fig. 14), the carbon isotopic record shows discrepancies with the global record of Cramer et al. (2009; Fig. 14). Large-scale shifts are observed in the marlstones of the Ainsa basin ($\delta^{13}C$ varying between -3 and 0.56 ‰; Fig. 11) suggesting a local imprint in the context of a rather stable global carbon isotopic record ($\delta^{13}C$ varying between 0.38 and 1.2‰; Cramer et al., 2009 recalibrated to GTS2012 by Grossman, 2012) during the deposition of the Hecho Group (*ca* 50.5 to 42 Ma, Fig. 14). Despite this difference between global and local isotopic records, a robust correlation is found between the sea-level and the stable carbon isotope curve from Fosado SGF system to Banaston SGF system (R=0.81, Castelltort et al., 2017; Fig. 14). To explain the observed correlation between negative (respectively positive) carbon isotope excursions and sea-level regressions (respectively transgressions), Castelltort et al. (2017) invoke the flux of fresh waters with low $\delta^{13}C$ DIC to the site of deposition during lowstands, and higher $\delta^{13}C$ DIC during transgression due to the enhanced burial of organic matter (depleted in ^{13}C) on the shelf (Jenkyns, 1996).

In the new isotopic dataset presented here (record from Banaston II? SGF system to the distal deposits of the Sobrarbe deltaic complex, see Fig. 14), trends highlighted in Castelltort et al. (2017) can still be recognized for most of the SGF systems.

(1) Banaston-II? shows a positive excursion during a sea-level highstand coherent with the patterns found in Castelltort et al. (2017; point 1 in Figs. 9 and 14). It is interesting to note that B-II? lateral deposits are related to an input of reworked, eroded or oxidized organic matter (type IV kerogen, Fig. 9). Chemical and/or biological oxidation of organic matter can induce a ^{13}C fractionation and an increase of $\delta^{13}C_{org}$ value of the residual organic carbon. Respectively, a decrease in the $\delta^{13}C$ of DIC can be observed leading to the recrystallization or the neoformation of carbonates phases with lower $\delta^{13}C$ values (e.g., DeNiro and Epstein, 1977; Jenkyns and Clayton, 1986). Here, we can safely exclude a distortion of the isotopic signal by chemical or biological oxidation as our data show the opposite trend with high $\delta^{13}C$ values associated to oxidized organic matter.

(2) Banaston-III to VI SGF systems are characterized by a negative $\delta^{13}C$ excursion and could be associated with the initiation of a global regression (point 2, in Figs. 9 and Fig. 14). The sharp transition from a positive $\delta^{13}C$ excursion for B-II? to a negative excursion for B-III is coeval with an increase in grain size (See *Supplementary material I, Fig.S.4.1.*, Si/Al, Ti/Al and Zr/Al ratios) and

takes place close to a turning point in the sea-level curve (Fig. 14). A decrease in the sea-level could enhanced the flux of fresh waters depleted in δ^{13}C DIC to deep marine settings and lead to a negative δ^{13}C excursion. In addition, a decrease in sea-level could enhance the flux of coarse grains as suggested by the increase in grain size.

(3) In the sandbodies of Ainsa SGF systems (A-I and A-II, point 3 in Figs. 9 and 14), the measured negative δ^{13}C excursion is coupled with a global regression as predicted by the systematic trend found in Castelltort et al. (2017).

(4) The marlstone interval between Ainsa II and the heterolithic beds identified at the top of the Forcaz section (point 4 in Figs. 9 and 14), displays a gradual increase in δ^{13}C. Two scenarios could produce such trend. The first scenario inculpates the sea-level as responsible for the gradual increase in δ^{13}C. Although our age model is poorly constrained for this interval, our geochemical data point toward deposition during the transgression characterizing the end of C20r, directly after the sea-level turning point of 44.8 Ma. The marlstones overlapping Ainsa II are marked by a net increase in Hi values (Fig. 11, red rectangle) and the repeated occurrence of type II kerogen indicates higher sea influence (Fig. 9). In addition, a progressive increase in δ^{13}C values and a general fining-upward (see *Supplementary material I, Fig.S.4.1.*, Si/Al, Ti/Al and Zr/Al ratios) would be consistent with more storage of organic matter and coarse sediments on the shelf as the sea-level rises. The second scenario inculpates an increase in the concentration of extrabasinal carbonates grains in deep marine deposits as highlighted by the petrographic study of Gupta and Pickering (2008). The flux of extrabasinal carbonates grains, still minor during the deposition of the Ainsa SGF system, became the main source of carbonate grains during the deposition of Morillo and Guaso SGF systems (Gupta and Pickering, 2008). The progressive increase in the δ^{13}C could thus reflect the enrichment through times in extrabasinal grains with high δ^{13}C values. In this second scenario, the correlation between our δ^{13}C and the sea-level would be a coincidence.

(5) From Morillo SGF system to the Sobrarbe deltaic complex (point 5 in Figs. 9 and 14), the isotope signal does not mirror the trends predicted by Castelltort et al. (2017). High δ^{13}C values are here linked to a global regression. Again, two scenarios could explain such record. In the first scenario, higher δ^{13}C values could be linked to the burial of organic matter during more severe anoxic conditions induced by the growth of the Boltaña anticline and restricted water circulation in the basin (Heard et al., 2008). Here, higher TOC are recorded in the marlstones of Morillo and Guaso (0.32 wt. % vs preceding 0.24 wt. % in average, Fig. 9). Rapid burial rates and a decrease in the oxidation of the organic matter could induce higher δ^{13}C by the sequestration of the ^{12}C in the organic matter (Jenkyns and Clayton, 1986), resulting in a positive excursion of the DIC and of the authigenic carbonates. The occurrence of major darker levels (e.g. San Lino level) supports this hypothesis. In addition, a decrease in the oxygenation of the basin was suggested by the Th/U values of Cantalejo and Pickering (2015) for Morillo and Guaso SGF systems. Finally, our Hi values show negative values during the Guaso SGF suggesting a higher input of terrestrial organic matter. Testing deeper this scenario would require δ^{13}C$_{org}$ measurements not performed within the scope of this study. In the second scenario, the high δ^{13}C values are again linked to the high proportion of extrabasinal carbonate grains. Gupta and Pickering (2008) showed the generally high proportion of extrabasinal carbonates grains (dolostones and micritic limestones) for Morillo and Guaso systems. A different δ^{13}C signature of the extrabasinal grains could lead to the overall high isotopic ratio recorded for these systems.

In conclusion, our isotopic data seems to indicated that the relation between sea-level and the stable carbon record highlighted in Castelltort et al. (2017) is robust if the basin in not affected by external sources of carbonates and/or water circulation restriction due to a confinement of the basin. It is interesting to note that our isotopic systems seem to respond quite fast to a change in sea-level as shown by the drastic decrease in the δ^{13}C associated to the turning point in the sea-level curve at around 47.5 Ma (Miller et al., 2005; Kominz et al., 2008).

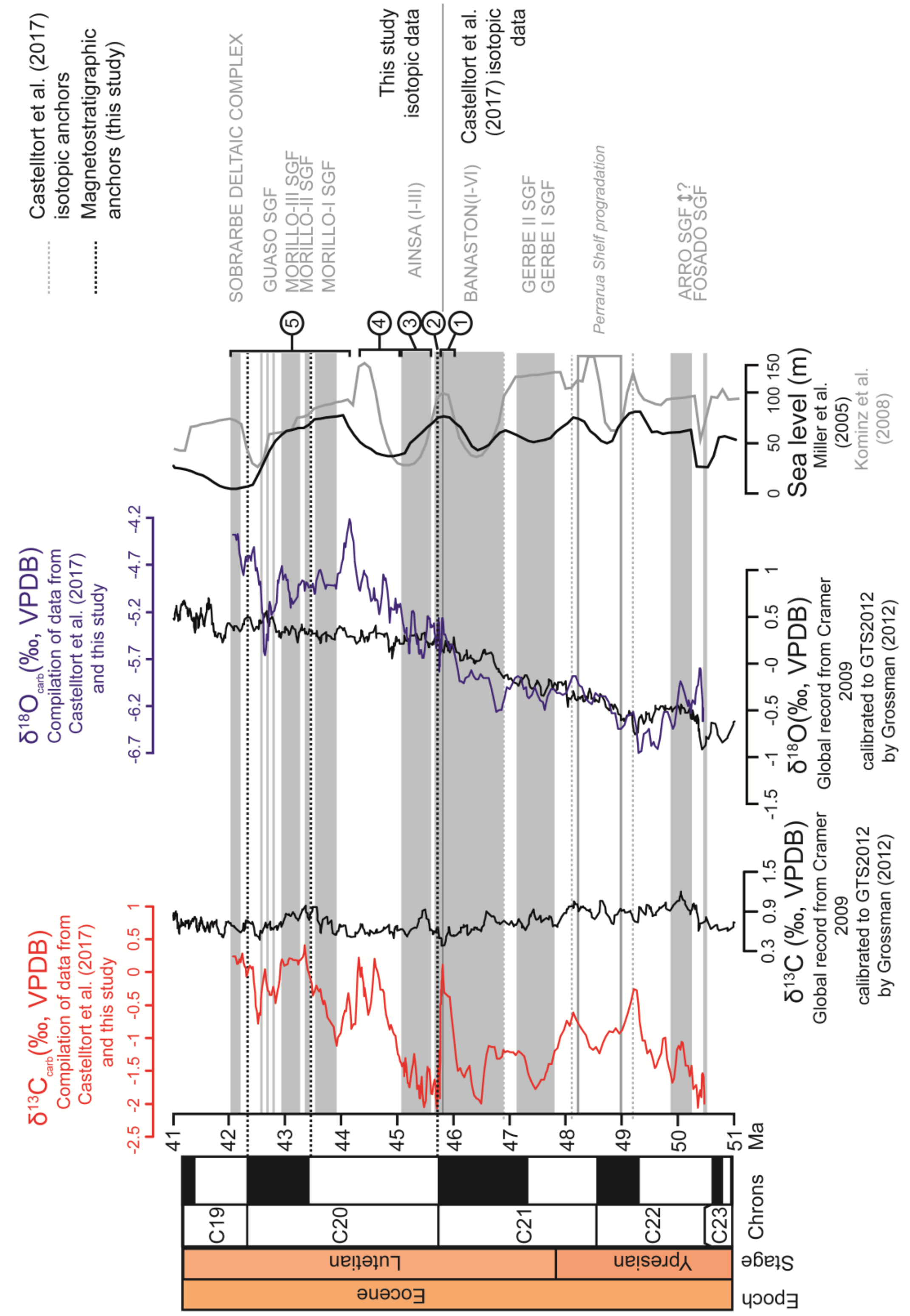

Figure 14. Comparison of isotopic values calibrated and global records (Isotopes: Cramer et al., 2009; Sea-level: Miller *et al.*, 2005 and Kominz et al., 2008). Note the link between lowstands /regression and activity of SGFs. Numbers on the right refer to points mentioned in sec. 5.2.2.. Global records are indicated with a 9-points mobile averages when the local dataset is displayed with a 5 points-moving average.

5.3 Pulses of sand delivery versus global sea-level record

The structural conditions during the deposition of the Hecho Group in the Ainsa basin are well constrained (Vinyoles et al., 2020). In more details, the deposition of Fosado SGF system is coeval with the major fluvial progradation and incision of the Castissent Fm linked, in literature, to thrust activities, a pulse in exhumation rates (Puigdefàbregas et al., 1986; Whitchurch et al., 2011; Chanvry et al., 2018) and a sea-level fall/lowstand (Marzo et al., 1988; Pickering and Bayliss, 2009; Castelltort et al., 2017). Still sourced from the Castissent Fm, the Arro SGF system is deposited during a sea-level highstand in Castelltort et al. (2017). Castelltort et al. (2017) hypothesized the deposition of the Arro SGFs to be driven by an increase of exhumation rates in the Pyrenees. This hypothesis was refined by Thomson et al. (2017)'s detrital zircon (U-Th)/He ages suggesting rather a short-frequency climatic or tectonic pulse. Recently, Cantalejo et al. (2020) suggested a younger age for the Arro system by the identification of the nannofossil Subzone NP14a, making more difficult a direct linkage between stratigraphy and eustatism.

Gerbe I and II are the response to the Montsec thrust sheet emplacement and the significant rate of relief growth in the Axial zone and this system is linked to the deposition of the Campanue Conglomerates (Mutti et al., 1985; Muñoz et al., 2013; Arbués et al., 2011; Scotchman et al., 2015). Finally, the remaining systems of the Hecho Group in the Ainsa basin are deposited during the growth of the Mediano and the Boltaña anticlines associated to the Sobrarbe Fold system (Muñoz et al., 2013). In these structural conditions controlling the large geometries of deposition, the accommodation and the supply of sediments to the shelf, a comparison of global sea-level curves and the stratigraphic records of the Ainsa basin still suggests eustasy as an important driver in delivering coarse sediment to deep-waters. In the Pueyo off-axis section tuned by the isotopic record, Fosado, Gerbe I and II and Banaston I members are systematically deposited during sea-level lowstands. Additionally, Banaston III to IV, Ainsa, Morillo and Guaso systems are deposited during regressive events. In more details, Banaston III to VI and the Ainsa members were deposited during the regressive event from *ca* 45.8 Ma to 44.9 Ma (Fig. 14). Morillo, Guaso SGF systems and the distal deposits of the Sobrarbe deltaic complex were deposited between 44 Ma to 42 Ma, during the subsequent regressive event (Fig. 14). The only exceptions to these systematic depositions during sea-level regression and lowstands are the Arro SGF system (see above) and Banaston II? member, possibly associated with a sea-level rise and/or a highstand. Interestingly, Gupta and Pickering (2008) showed an enrichment of these two systems in intrabasinal carbonate in comparison to the remaining systems of the basin. Intrabasinal carbonate grains are sourced from coeval carbonates platforms on the shelf and/or the erosion of older carbonates by the growth of the Mediano and Boltaña structure (Gupta and Pickering, 2008). The growth of these tectonic structures could explain the deposition of B-II? system in the context of a high sea-level stand. Finally, the thick marlstones interval found between Ainsa and Morillo (point 4 in Figs. 9 and 14) is associated with an extensive transgressive period. The systematic deposition of sandstones enriched sediments during sea-level lowstands or regressive events, and vice versa thick marlstone interval during transgressive events, suggests that, in the Ainsa basin sedimentary fill, clastic sediments responded strongly to global eustatic variations.

6. Conclusions

We highlight the importance of studying deep-sea environments by a multi-proxy approach in order to disentangle complex signals recorded in settings (such as the deep-marine) with a high preservation potential.

This study provides a new age model for the deep marine sediment gravity flow deposits of the upper Hecho Group (from Banaston SGF system to the distal deposits of the Sobrarbe deltaic complex) in the Ainsa basin (southern central Pyrenees). It integrates Castelltort et al. (2017) dataset (from Fosado to Banaston SGFs) with new chronostratigraphic constraints (by magnetostratigraphy and biostratigraphy) for Banaston SGFs to the distal deposits of the Sobrarbe deltaic complex in the deep marine stratigraphic series of the Ainsa basin.

New magnetostratigraphic data are corroborated by biostratigraphy suggesting magnetozones C21n, C20r, C20n and C19r for the sediments deposited from Banaston SGFs to the Sobrarbe deltaic complex. New biostratigraphic sites strengthened this interpretation with the detection of NP16 for two sites in the Guaso SGF system. Our new integrated data indicate a deposition age of 45.72 Ma for

Banaston IV SGF system, 43.43 Ma for Morillo II SGF system and 42.3 Ma for the distal deposits of the Sobrarbe delta. These results give relative constant net sediment accumulation rates of (1) 54.1 cm/kyr between Banaston III or IV and Morillo II, and (2) 51.5 cm/kyr between Morillo II and the distal members of the Sobrarbe delta.

These chronostratigraphic constraints were used to correlate isotopic datasets and compare them with global “targets” curves. While oxygen isotope mirrors the global trend, the carbon isotope local signal seems to be controlled by sea-level modulations as long as the waters circulation is not restricted and/or as long as extrabasinal carbonate grains stay a minor component of the sediments accumulating in the basin. A mismatch between the local isotopic curve and the eustatic variations as predicted by Castelltort et al., 2017 is thus observed for Morillo and Guaso SGF systems that might be explained by the presence of extrabasinal carbonate grains or a partial restriction in water circulation

Finally, despite the complex tectonic setting of the Ainsa basin during the deposition of the Hecho Group, a systematic trend can be detected between the deposition of sandstones enriched sediments and global eustatic variations. Most SGF systems (Fosado, Gerbe, Ainsa, Morillo and Guaso) and the distal deposits of the Sobrarbe deltaic complex are systematically deposited during sea-level falls or lowstands. Respectively, major marlstones intervals are deposited during transgressive events. The only exceptions might be Arro SGF system possibly associated to a climatic and a tectonic pulse, and Banaston II associated to the growth of tectonic structures in the basin.

Acknowledgements

This work was supported by an Augustin Lombard Grant from the SPHN Society of Geneva [grant Augustin Lombard, 2016, to Läuchli], a Equinor grant to Castelltort and a MINECO spanish project CGL2014-55900 to Garcés. Thanks to the Paleomagnetic Laboratory CCiTUB-ICTJA CSIC where the paleomagnetic analyses were conducted. Many thanks also to Fabio Capponi for XRF analysis and Andreu Vinyoles for support on the field.

Data availability

Datasets presented in this article will be found in the *Supplementary material II* associated with the published manuscript.

Supplementary material

Supplementary material I: S.1.Material and methods; S.2. Supplementary material for magnetostratigraphy; S.3. Detailed biostratiraphic results; S.4. Elemental and mineralogic composition of the sediments

Supplementary material II: datasets

References

Arbués, P., D. Mellere, O. Falivene, O. Fernández-Bellón, J. A. Muñoz, M. Marzo, de Gibert, J.M., 2007, Context and architecture of the Ainsa-1-quarry channel complex, Spain, in Atlas of Deep-Water Outcrops, edited by T. H. Nilsen et al. AAPG Studies in Geology, vol. 56, CD-ROM, 20 pp ,AAPG-Shell Explor. and Prod., Tulsa, Okla.

Arbués, P., Butillé, M., López-Blanco, M., Marzo, M., Monleón, O., Muñoz, J.A., Serra-Kiel, J. 2011. Exploring the relationships between deepwater and shallow-marine deposits in the Aínsa piggy back basin fill (Eocene, South Pyrenean Foreland Basins). In Post-Meeting Field Trips Guidebook, 28th IAS Meeting, Zaragoza, Arenas, C., Pomar, L., Colombo, F. (eds). Sociedad Geológica de España: Salamanca, Spain. Geo-Guías 8,199–238.

Barnolas, A., Gil-Peña, I., 2001. Ejemplos de relleno sedimentario multiepisódico en una cuenca de antepaís fragmentada: La Cuenca Surpirenaica. Boletín Geológico y Minero, 112(3), 17-38.

Beaumont, C., Muñoz, J. A., Hamilton, J., Fullsack, P., 2000. Factors controlling the Alpine evolution of the central Pyrenees inferred from a comparison of observations and geodynamical models. Journal of Geophysical Research: Solid Earth, 105(B4), 8121–8145. https://doi.org/10.1029/1999JB900390

Bentham, P.A., 1992. The tectono-stratigraphic development of the western oblique ramp of the south-central Pyrenean thrust system, Northern Spain. Ph. D. thesis, University of Southern California, 253.

Bentham, P.A, Burbank, D.W., Puigdefàbregas, C., 1992. Temporal and spatial controls on the alluvial architecture of an axial drainage system: late Eocene Escanilla Formation, southern Pyrenean foreland basin, Spain. Basin Research, 4, 335-352.

Bentham, P., Burbank, D.W., 1996. Chronology of Eocene foreland basin evolution along the western oblique margin of the South-Central Pyrenees.In: Friend, P.F., Dabrio, C.J. (eds) Tertiary basins of Spain. The Stratigraphic Record of Curstal Kinematics, Cambridge University Press, 144–152.

Bouma, A.H., Normark, W.R., Barnes, N.E., 1985. Submarine Fans and Related Turbidite Systems. (eds) Berlin, Springer-Verlag, 343 p.

Boscolo Galazzo, F., Thomas, E., Pagani, M., Warren, C., Luciani, V., Giusberti, L., 2014. The middle Eocene climatic optimum (MECO): A multiproxy record of paleoceanographic changes in the southeast Atlantic (ODP Site 1263, Walvis Ridge). Paleoceanography, 29(12), 1143–1161. https://doi.org/10.1002/2014PA002670

Cantalejo, B., Pickering, K. T., 2014. Climate forcing of fine-grained deep-marine systems in an active tectonic setting: Middle Eocene, Ainsa Basin, Spanish Pyrenees. Palaeogeography, Palaeoclimatology, Palaeoecology, 410, 351–371. https://doi.org/10.1016/j.palaeo.2014.06.005

Cantalejo, B., Pickering, K. T., 2015. Orbital forcing as principal driver for fine-grained deep-marine siliciclastic sedimentation, Middle-Eocene Ainsa Basin, Spanish Pyrenees. Palaeogeography, Palaeoclimatology, Palaeoecology, 421, 24–47. https://doi.org/10.1016/j.palaeo.2015.01.008

Cantalejo, B., Pickering, K.T., McNiocaill, C., Bown, P., Johansen, K., Grant, M., 2020. A revised age-model for the Eocene deep-marine siliciclastic systems, Ainsa Basin, Spanish Pyrenees. Journal of the Geological Society, https://doi.org/10.1144/jgs2019-131

Castelltort, S., Van Den Driessche, J., 2003. How plausible are high-frequency sediment supply-driven cycles in the stratigraphic record?. Sedimentary Geology, 157(1-2), 3-13. https://doi.org/10.1016/S0037-0738(03)00066-6

Castelltort, S., Honegger, L., Adatte, T., Clark, J. D., Puigdefàbregas, C., Spangenberg, J. E., Dykstra M. L., Fildani, A., 2017. Detecting eustatic and tectonic signals with carbon isotopes in deep-marine strata, Eocene Ainsa Basin, Spanish Pyrenees. Geology, 45(8), 707–710. https://doi.org/10.1130/G39068.1

[dataset] Castelltort, S., Honegger, L., Adatte, T., Clark, J. D., Puigdefàbregas, C., Spangenberg, J. E., Dykstra M. L., Fildani, A., 2017. Detecting eustatic and tectonic signals with carbon isotopes in deep-marine strata, Eocene Ainsa Basin, Spanish Pyrenees. Supplementary material, GSA Data Repository item 2017228, http://www.geosociety.org/datarepository/2017/

Chanvry, E., Deschamps, R., Joseph, P., Puigdefàbregas, C., Poyatos-Moré, M., Serra-Kiel, J., Garcia, D., Teinturier, S., 2018. The influence of intrabasinal tectonics in the stratigraphic evolution of piggyback basin fills: Towards a model from the Tremp-Graus-Ainsa Basin (South-Pyrenean Zone, Spain). Sedimentary geology, 377, 34-62.

Choukroune, P., 1992. Tectonic evolution of the Pyrenees. Annual Review of Earth and Planetary Sciences, 20, 143–158.

Clark, J., Puigdefàbregas, C., Castelltort, S., Fildani, A., 2017. Propagation of Environmental Signals Within Source-to-sink Stratigraphy: Spanish Pyrenees, June 5th-9th, 2017. (eds.) SEPM (Society for Sedimentary Geology).

Cornard, P. H., Pickering, K. T., 2019. Supercritical-flow Deposits and Their Distribution in a Submarine Channel System, Middle Eocene, Ainsa Basin, Spanish Pyrenees. Journal of Sedimentary Research, 89(6), 576-597. https://doi.org/10.2110/jsr.2019.34

Costa, E., Garcés, M., López-Blanco, M., Beamud, E., Gómez-Paccard, M., Larrasoaña, J. C., 2010. Closing and continentalization of the South Pyrenean foreland basin (NE Spain): Magnetochronological constraints. Basin Research, 22, 904–917.

Covault, J. A., Normark, W.R., Romans, B.W., Graham, S.A., 2007. Highstand fans in the California borderland: The overlooked deep-water depositional systems. Geology, 35(9), 783-786. https://doi.org/10.1130/G23800A.1

Covault, J. A., Graham, S. A., 2010. Submarine fans at all sea-level stands: Tectono-morphologic and climatic controls on terrigenous sediment delivery to the deep sea. Geology, 38(10), 939-942. https://doi.org/10.1130/G31081.1

Cramer, B. S., Toggweiler, J. R., Wright, J. D., Katz, M. E., Miller, K. G., 2009. Ocean overturning since the Late Cretaceous: Inferences from a new benthic foraminiferal isotope compilation. Paleoceanography, 24(4), 1–14. https://doi.org/10.1029/2008PA001683

De Federico, A., 1981. La sedimentación de talud en el sector occidental de la cuenca Paleógena de Aínsa. Universidad Autonoma de Barcelona Publicaciones de Geologia 12, 271.

DeNiro, M. J., Epstein, S., 1977. Mechanism of carbon isotope fractionation associated with lipid synthesis. Science, 197(4300), 261-263.

Dreyer, T., Corregidor, J., Arbues, P., Puigdefàbregas, C., 1999. Architecture of the tectonically influenced Sobrarbe deltaic complex in the Ainsa Basin, northern Spain. Sedimentary Geology, 127(3–4), 127–169. https://doi.org/10.1016/S0037-0738(99)00056-1

Fernández, O., Muñoz, J. A., Arbués, P., Falivene, O., 2012. 3D structure and evolution of an oblique system of relaying folds: the Ainsa basin (Spanish Pyrenees). Journal of the Geological Society, 169(5), 545-559. https://doi.org/10.1144/0016-76492011-068

Fillon, C., van der Beek, P., 2012. Post-orogenic evolution of the southern Pyrenees: Constraints from inverse thermo-kinematic modelling of low-temperature thermochronology data. Basin Research, 24(4), 418–436. https://doi.org/10.1111/j.1365-2117.2011.00533.x

Garcés, M., López-Blanco, M., Valero, L., Beamud, E., Muñoz, J.A., Oliva-Urcia, B., Vinyoles, A., Arbués, P., Cabello, P. Cabrera, L., 2020. Paleogeographic and sedimentary evolution of the South Pyrenean foreland basin. Marine and Petroleum Geology, *113*, p.104105. https://doi.org/10.1016/j.marpetgeo.2019.104105

Gómez-Gras, D., Roigé, M., Fondevilla, V., Oms, O., Boya, S., Remacha, E., 2016. Provenance constraints on the Tremp Formation paleogeography (southern Pyrenees): Ebro Massif VS Pyrenees sources. Cretaceous Research, 57, 414-427.

Gradstein, F. M., Ogg, J. G., Schmitz, M., Ogg, G. (Eds.)., 2012. The geologic time scale 2012. Elsevier, 2-Volume Set, 1st Edition.

Grossman, E. L., 2012. Chapter 10. Oxygen isotope stratigraphy. In: Geological Time Scale 2012, Gradstein, F& Ogg, J (eds.), 2-Volume Set, 1st Edition, Elsevier. ISBN: 9780444594259

[dataset] Grossman, E. L., 2012. Geological Time Scale 2012. Chapter 10. Oxygen isotope stratigraphy. In: Geological Time Scale 2012, Gradstein, F& Ogg, J (eds.), 2-Volume Set, 1st Edition, Elsevier. Appendix 1., PANGEA, https://doi.org/10.1594/PANGAEA.776989

Gupta, K. D., Pickering, K. T., 2008. Petrography and temporal changes in petrofacies of deep-marine Ainsa–Jaca basin sandstone systems, Early and Middle Eocene, Spanish Pyrenees. Sedimentology, 55(4), 1083-1114.

Heard, T. G., Pickering, K. T., 2008. Trace fossils as diagnostic indicators of deep-marine environments, Middle Eocene Ainsa-Jaca basin, Spanish Pyrenees. Sedimentology, 55(4), 809–844. https://doi.org/10.1111/j.1365-3091.2007.00922.x

Heard, T. G., Pickering, K. T., Robinson, S. A., 2008. Milankovitch forcing of bioturbation intensity in deep-marine thin-bedded siliciclastic turbidites. Earth and Planetary Science Letters, 272(1–2), 130–138. https://doi.org/10.1016/j.epsl.2008.04.025

Hessler, A. M., Fildani, A., 2019. Deep-sea fans: tapping into Earth's changing landscapes. Journal of Sedimentary Research, 89(11), 1171-1179.

Holl, J. E., Anastasio, D. J., 1993. Paleomagnetically derived folding rates, southern Pyrenees, Spain. Geology, 21 (3), 271–274.

Irwin, H., Curtis, C., Coleman, M., 1977. Isotopic evidence for source of diagenetic carbonates formed during burial of organic-rich sediments. Nature, 269(5625), 209-213.

Jenkyns, H. C., 1996. Relative sea-level change and carbon isotopes: Data from the upper Jurassic (Oxfordian) of central and Southern Europe. Terra Nova, 8(1), 75-85. https://doi.org/10.1111/j.1365-3121.1996.tb00727.x

Jenkyns, H. C., Clayton, C. J., 1986. Black shales and carbon isotopes in pelagic sediments from the Tethyan Lower Jurassic. Sedimentology, *33*(1), 87-106. https://doi.org/10.1111/j.1365-3091.1986.tb00746.x

Jones, R.W., Pickering, K.T., Boudagher-Fadel, M.,Matthews, S., 2005. Preliminary observations on the micropalaeontological characterization of submarine fan/channel subenvironments, Ainsa System, south-central Pyrenees, Spain. In: Powell, A. J., Riding, J.B. (eds), Recent Developments in Applied Biostratigraphy,The Micropalaeontological Society, Special Publication, 1 (2005), 55-68.

Kominz, M.A., Browning, J.V., Miller, K.G., Sugarman, P.J., Mizintseva, S., and Scotese, C.R., 2008. Late Cretaceous to Miocene sea-level estimates from the New Jersey and Delaware coastal plain coreholes: An error analysis. Basin Research, 20, 211–226. doi: 10 .1111 /j .1365 -2117 .2008 .00354 .x.

Labaume, P., Teixell, A., 2018. 3D structure of subsurface thrusts in the eastern Jaca Basin, southern Pyrenees. *Geologica Acta*, *16*(4), 477-498. https://doi.org/10.1344/GeologicaActa2018.16.4.9

Lisiecki, L.E., Raymo, M.E., 2005. A Pliocene-Pleistocene stack of 57 globally distributed benthic d18O records. Paleoceanography 20 (1), https://doi.org/10.1029/2004PA001071.

Marzo, M., Nijman, W., Puigdefàbregas, C., 1988. Architecture of the Castissent fluvial sheet sandstones, Eocene, south Pyrenees, Spain. Sedimentology, 35(5), 719-738.

McCarthy, K., Rojas, K., Niemann, M., Palmowski, D., Peters, K., Stankiewicz, A., 2011. Basic Petroleum Geochemistry for Source Rock Evaluation. Oilfield Review, 23(2), 32–43. https://doi.org/10.1016/j.epsl.2006.01.027

Mey, P.H.W., Nagtegaal, P.J.C., Roberti, K.J., Hartevelt, J.J.A., 1968. Lithostratigraphic subdivision of post-Hercynian deposits in the south-central Pyrenees, Spain. Leidse Geologische Mededelingen, v. 41, no. 1, p. 221–228.

Michael, N. A., Whittaker, A. C., Carter, A., Allen, P. A., 2014. Volumetric budget and grain-size fractionation of a geological sediment routing system: Eocene Escanilla Formation, south-central Pyrenees. Bulletin of the Geological Society of America, 126(3-4), 585-599. https://doi.org/10.1130/B30954.1

Miller, K. G., Kominz, M. A., Browning, J. V., Wright, J. D., Mountain, G. S., Katz, M. E., Sugarman, P.J., Cramer, B.S., Christie-Blick, N., Pekar, S. F., 2005. The Phanerozoic record of global sea-level change. Science, 310 (5752), 1293–1298. https://doi.org/10.1126/science.1116412

Mochales, T., Barnolas, A., Pueyo, E. L., Serra-Kiel, J., Casas, A. M., Samsó, J. M., Sanjuán, J., 2012a. Chronostratigraphy of the boltaña anticline and the Ainsa Basin (southern pyrenees). Bulletin of the Geological Society of America, 124(7–8), 1229–1250. https://doi.org/10.1130/B30418.1

Mouthereau, F., Filleaudeau, P. Y., Vacherat, A., Pik, R., Lacombe, O., Fellin, M. G., Castelltort, S., Christophoul, F., Masini, E., 2014. Placing limits to shortening evolution in the Pyrenees: Role of margin architecture and implications for the Iberia/Europe convergence. Tectonics, 33(12), 2283–2314. https://doi.org/10.1002/2014TC003663

Muñoz, J. A., 1992. Evolution of a continental collision belt: ECORS-Pyrenees crustal balanced cross-section. In: McClay K.R. (eds) Thrust Tectonics. Springer, Dordrecht, 235–246. https://doi.org/10.1007/978-94-011-3066-0_21

Muñoz, J. A., Beamud, E., Fernández, O., Arbués, P., Dinarès-Turell, J., Poblet, J., 2013. The Ainsa Fold and thrust oblique zone of the central Pyrenees: Kinematics of a curved contractional system from paleomagnetic and structural data. Tectonics, 32(5), 1142–1175. https://doi.org/10.1002/tect.20070

Muñoz, J. A., Mencos, J., Roca, E., Carrera, N., Gratacós, O., Ferrer, O., Fernández, O., 2018. The structure of the South-Central-Pyrenean fold and thrust belt as constrained by subsurface data. Geologica Acta, 16(4), 439-460. https://doi.org/10.1344/GeologicaActa2018.16.4.7

Mutti, E., Luterbacher, H.P., Ferrer, J., Rossell, J., 1972. Schema stratigrafico e lineamenti di facies del Paleogenemarino della zona centrale sudpirenaica tra Tremp (Catalogna) e Pamplona (Navarra). Mem. Soc. Geol. Ital. 11, 391–416.

Mutti, E., 1983. The Hecho Eocene submarine fan system, south-central Pyrenees, Spain. Geo- Marine Letters, 3, 199–202. https://doi.org/10.1007/BF02462468

Mutti, E., Remacha, E., Sgavetti, M., Rosell, J., Valloni, R., Zamorano,M., 1985. Stratigraphy and facies characteristics of the Eocene Hecho Group turbidite systems, south-central Pyrenees. In: Mila, M.D., Rosell (eds) Excursion Guidebook of the 6th European Regional Meeting, International Association of Sedimentologists, Lleida, Spain. 519–576.

Mutti, E., Séguret, M., and Sgavetti, M., 1988. Sedimentation and deformation in the Tertiary sequences of the southern Pyrenees: Field trip 7: Parma, Italy. University of Parma, 1-30.

Nijman, W., 1998. Cyclicity and basin axis shift in a piggyback basin: towards modelling of the Eocene Tremp-Ager Basin, South Pyrenees, Spain. Geol. Soc. Lond., Spec. Publ. 134 (1), 135–162.

Nijman,W., Nio, S.D., 1975. The Eocene Montanana Delta (Tremp-Graus Basin, Provinces Lerida and Huesca, Southern Pyrenees, N. Spain). In: Rosell, J., Puigdefàbregas, C. (Eds.), 9th International Sedimentological Congress International Association of Sedimentologists, Nice.

Ogg, J., Lugowski, A., 2020. TS Creator visualization of enhanced Geologic Time Scale 2004 database (Version 6.8), http://www.tscreator.org

Payros, A., Tosquella, J., Bernaola, G., Dinarès-Turell, J., Orue-Etxebarria, X., Pujalte, V., 2009. Filling the North European Early/Middle Eocene (Ypresian/Lutetian) boundary gap: Insights from the Pyrenean continental to deep-marine record. Palaeogeography, Palaeoclimatology, Palaeoecology, 280(3–4), 313–332. https://doi.org/10.1016/j.palaeo.2009.06.018

Pekar, S. F., Hucks, A., Fuller, M., Li, S., 2005. Glacioeustatic changes in the early and middle Eocene (51-42 Ma): Shallow-water stratigraphy from ODP Leg 189 Site 1171 (South Tasman Rise) and deep-sea $\delta18O$ records. Bulletin of the Geological Society of America, 117(7–8), 1081–1093. https://doi.org/10.1130/B25486.1

Pickering, K. T., Corregidor, J., 2005. Mass-transport complexes (MTCs) and tectonic control on basin-floor submarine fans, middle Eocene, south Spanish Pyrenees. Journal of Sedimentary Research, 75(5), 761–783. https://doi.org/10.2110/jsr.2005.062

Pickering, K. T., Bayliss, N. J., 2009. Deconvolving tectono-climatic signals in deep-marine siliciclastics, Eocene Ainsa basin, Spanish Pyrenees: Seesaw tectonics versus eustasy. Geology, 37(3), 203–206. https://doi.org/10.1130/G25261A.1

Piper, D.J.W., Normark, W.R., 2001. Sandy fans: from Amazon to Hueneme and beyond. American Association of Petroleum Geologists, Bulletin, v. 85, p. 1407–1438.

Pohl, F., McCann, T., 2014. Architecture and depositional development of the Eocene deep-marine Morillo and Coscojuela Formations, Aínsa Basin, Spain. Geological Journal, 49(3), 221–238. https://doi.org/10.1002/gj.2511

Posamentier, H. W., Vail, P. R., 1988. Eustatic controls on clastic deposition II—Sequence and systems tract models, (42). In: Wilgus, C.K., Hastings, B.S., Kendall, C.G.S.C., Posamentier, H.W., Ross, C.A., Van Wagoner J.C. (eds) Sea-Level Changes: an Integrated Approach, SEPM Special Publication, 42, 125-154.

Poblet, J., J. A. Muñoz, A. Travé, and J. Serra-Kiel, 1998. Quantifying the kinematics of detachment folds using three-dimensional geometry: Application to the Mediano anticline (Pyrenees, Spain). Geol. Soc. Am. Bull., 110(1), 111–125. doi: https://doi.org/10.1130/0016-7606(1998)110<0111:QTKODF>2.3.CO;2

Puigdefàbregas, C., 1975. La Sedimentación Molásica en la Cuenca de Jaca. Pirineos, 104, 1–188.

Puigdefàbregas, C., Souquet, P., 1986. Tecto-sedimentary cycles and depositional sequences of the Mesozoic and Tertiary from the Pyrenees. Tectonophysics, 129(1–4), 173–203. https://doi.org/10.1016/0040-1951(86)90251-9

Puigdefàbregas, C., Muñoz, J.A., Vergés, J., 1992. Thrusting and foreland basin evolution in the Southern Pyrenees. In: McClay K.R. (eds) Thrust Tectonics Springer, Dordrecht, 247-254.

Pujalte, V., Schmitz, B., 2005. Revisión de la estratigrafía del Grupo Tremp («Garumniense», Cuenca de Tremp-Graus, Pirineos meridionales). Geogaceta, 38(79), e82.

Remacha, E., Fernández, L.P., 2003. High-resolution correlation patterns in the turbidite systems of the Hecho Group (South-Central Pyrenees, Spain). Marine and Petroleum Geology. 20 (6–8), 711–726.

Romans, B. W., Castelltort, S., Covault, J. A., Fildani, A., Walsh, J. P., 2016. Environmental signal propagation in sedimentary systems across timescales. Earth-Science Reviews, 153, 7-29.

Rosenbaum, G., Lister, G. S., Duboz, C., 2002. Relative motions of Africa, Iberia and Europe during Alpine orogeny. Tectonophysics, 359(1-2), 117-129. https://doi.org/10.1016/S0040-1951(02)00442-0

Roure, F., Chourkroune, P., 1998. Contribution of the Ecors seismic data to the Pyrenean geology: Crustal architecture and geodynamic evolution of the Pyrenees. In: B. Damotte (eds) The ECORS Pyrenean Deep Seismic Surveys, 1985-1994, Mémoires de la Société géologique de France, 173, 37-52.

Schlager, W., 1993. Accommodation and supply—a dual control on stratigraphic sequences. Sedimentary geology, 86(1-2), 111-136. https://doi.org/10.1016/0037-0738(93)90136-S

Scotchman, J.I., Bown, P., Pickering, K.T., BouDagher-Fadel, M., Bayliss, N.J., Robinson, S.A., 2015. A new age model for the middle Eocene deep-marin Ainsa Basin, Spanish Pyrenees. Earth-Science Reviews,144, 10-20. http://dx.doi.org/10.1016/j.earscirev.2014.11.006

Scotchman, J. I., Pickering, K. T., Sutcliffe, C., Dakin, N., Armstrong, E., 2015. Milankovitch cyclicity within the middle Eocene deep-marine Guaso system, Ainsa Basin, Spanish Pyrenees. Earth-Science Reviews, 144, 107–121. https://doi.org/10.1016/j.earscirev.2015.01.007

Séguret, M., 1972. Étude tectonique des nappes et séries décollées de la partie centrale du versant sud des Pyrénées – caractère synsédimentaire, rôle de la compression et de la gravité, Série géologie structurale, 2, France. Publications de l'Université des Sciences et Techniques du Languedoc (USTELA), Montpellier, France, 155.

Sinclair, H. D., Gibson, M., Naylor, M., Morris, R. G., 2005. Asymmetric growth of the Pyrenees revealed through measurement and modeling of orogenic fluxes. American Journal of Science, 305(5), 369-406. doi: 10.2475/ajs.305.5.369

Sluijs, A., Zeebe, R. E., Bijl, P. K., Bohaty, S. M., 2013. A middle Eocene carbon cycle conundrum. Nature Geoscience, 6(6), 429-434.

Thomson, K. D., Stockli, D. F., Clark, J. D., Puigdefàbregas, C., Fildani, A., 2017. Detrital zircon (U-Th)/(He-Pb) double-dating constraints on provenance and foreland basin evolution of the Ainsa Basin, south-central Pyrenees, Spain. Tectonics, 36(7), 1352–1375. https://doi.org/10.1002/2017TC004504

Thomson, K. D., Stockli, D. F., Odlum, M. L., Tolentino, P., Puigdefàbregas, C., Clark, J., Fildani, A., 2019. Sediment provenance and routing evolution in the Late Cretaceous–Eocene Ager Basin, south-central Pyrenees, Spain. Basin Research. https://doi.org/10.1111/ bre.12376.

Tripati, A., Backman, J., Elderfield, H., Ferretti, P., 2005. Eocene bipolar glaciation associated with global carbon cycle changes. Nature, 436(7049), 341-346.

Vail, P.R., Mitchum Jr., R.M., Thompson III, S., 1977. Seismic stratigraphy and global changes of sea level, Part 3: relative changes of sea level from coastal onlap. In: Payton, C.E. (eds) Seismic Stratigraphy-Applications to Hydrocarbon Exploration, American Association of Petroleum Geologists Memoir, 26, 63-81.

Vinyoles, A., López-Blanco, M., Garcés, M., Arbués, P., Valero, L., Beamud, E., Oliva-Urcia, B. Cabello, P., 2019. 10 Myr evolution of sedimentation rates in a deep marine to non-marine foreland basin system: tectonic and sedimentary controls (Eocene, Tremp-Jaca Basin, Southern Pyrenees, NE Spain). Basin Research. https://doi.org/10.1111/bre.12481

Weltje, G., de Boer, P. L., 1993. Astronomically induced paleoclimatic oscillations reflected in Pliocene turbidite deposits on Corfu (Greece): implications for the interpretation of higher order cyclicity in ancient turbidite systems. Geology, 21(4), 307-310. https://doi.org/10.1130/0091-7613(1993)021<0307:AIPORI>2.3.CO;2

Westerhold, T., Röhl, U., 2013. Orbital pacing of Eocene climate during the Middle Eocene Climate Optimum and the chron C19r event: Missing link found in the tropical western Atlantic. Geochemistry, Geophysics, Geosystems, 14(11), 4811–4825. https://doi.org/10.1002/ggge.20293

Whitchurch, A. L., Carter, A., Sinclair, H. D., Duller, R. A., Whittaker, A. C., Allen, P. A., 2011. Sediment routing system evolution within a diachronously uplifting orogen: Insights from detrital zircon thermochronological analyses from the South-Central Pyrenees. American Journal of Science, 311(5), 442-482.

Zachos, J., Pagani, M., Sloan, L., Thomas, E., Billups, K., 2001. Trends, rhythms, and aberrations in global climate 65 Ma to present. Science, 292(5517), 686-693.